POLITECNICO DI MILANO

Scuola di Ingegneria dei Sistemi
Corso di Laurea Magistrale in Ingegneria Fisica
Dipartimento di Fisica

Spin-Orbit and Crystal Field Excitations in Cerium Compounds probed by Resonant Inelastic X-ray Scattering

Relatore: prof. Giacomo Claudio GHIRINGHELLI
Correlatore: dr. Kurt KUMMER

Tesi di laurea di:
Mauro FANCIULLI
matr. 782719

a.a. 2012-2013

It's a magical world, Hobbes, ol' buddy...
...let's go exploring!

Calvin

Spin-Orbit and Crystal Field Excitations in Cerium Compounds probed by Resonant Inelastic X-ray Scattering

Mauro Fanciulli

18^{th} December 2013

Abstract

In this thesis a study of low energy excitations in three Cerium intermetallics by means of soft X-ray Absorption Spectroscopy (XAS) and Resonant Inelastic X-ray Scattering (RIXS) is presented. Measurements were performed at beamline ID08 of the European Synchrotron Radiation Facility (ESRF).

Rare Earths materials are peculiar because the partially filled $4f$ shell is well localized at the atomic site but lies close to the Fermi level, thus being involved in transport properties. The $4f$ electronic structure of Rare Earth atoms is dominated by Spin-Orbit coupling, but the interaction with the non-spherical electrostatic field generated by the surrounding charges, called Crystal Field, produces a further splitting of the $(2j+1)$-fold degeneracy because of a lowering of symmetry. Among Rare Earths, Cerium atom has only one f electron, therefore Spin-Orbit splitting is into only two states: $^2F_{5/2}$ and $^2F_{7/2}$.

Aim of this work is to analyze the excitations involving two f levels, so-called ff excitations, by means of resonant soft X-ray scattering. The two levels can have a different total momentum J (Spin-Orbit excitations) or share the same J (Crystal Field excitations). For Cerium the former are expected to have ~ 300 meV of energy, the latter ~ 50 meV.

From absorption measurements we demonstrate a valence transition from Ce^{4+} to Ce^{3+} among the three samples, $Nd_{1.84}Ce_{0.16}CuO_4$, $CeCu_2Si_2$, $CeRu_2P_2$, thanks to a comparison with reference samples. Moreover, differences between Fluorescence Yield and Auger Electron Yield are discussed. X-ray Linear Dichroism is small, thus Crystal Field effects are small.

Scattering measurements in resonance with M_5 edge from Ce^{4+} sample show only the elastic line in the low energy range, as expected because no excitations shall take place in the empty $4f$ shell. In addition, a clear fluorescence feature in RIXS spectra is observed. On the other hand, scattering from Ce^{3+} reveals an inelastic feature ascribable to a Spin-Orbit excitation. Crystal Field excitations and a possible their dispersion with momentum are not well resolved; nevertheless an interesting clue is the broadening of RIXS features much larger than the spectrometer resolution, suggesting a Crystal Field substructure. Measurements on the M_4 edge show in addition a high energy loss due to Coster-Kronig conversion.

This is one of the very few works on Rare Earth compounds with RIXS, and for the first time hints of Crystal Field excitations were observed by means of X-ray scattering, previously domain of neutrons. This suggests that RIXS is a promising forefront technique with competitive properties respect to other kind of measures able to probe elementary low energy excitations in $4f$ materials, also in sight of the new incoming upgrades in energy and momentum resolution.

Estratto

Con questa Tesi viene presentato uno studio di eccitazioni a bassa energia in tre campioni intermetallici di Cerio. Gli esperimenti di assorbimento di raggi X (X-ray Absorption Spectroscopy, XAS) e di scattering risonante anelastico (Resonant Inelastic X-ray Scattering, RIXS) sono stati eseguiti nella beamline ID08 dell'European Synchrotron Radiation Facility (ESRF).

Nell'ultimo ventennio, a seguito della costruzione di sorgenti di radiazione di sincrotrone di terza generazione, e grazie allo sviluppo di diverse tecnologie avanzate nel campo dell'ottica di raggi X e dei detector di fotoni, la RIXS si è dimostrata una tra le migliori tecniche per l'analisi di eccitazioni fondamentali in campioni complessi. Difatti essa è l'unica ad avere, tra le sue proprietà, la capacità di selezionare sia la specie chimica sia il sito reticolare, di studiare campioni sia spessi sia sottili, e mantenere la neutralità della carica, trattandosi di una tecnica fotone in - fotone out.

La RIXS viene soprattutto impiegata nello studio della dipendenza dall'energia, dal momento trasferito e dalla polarizzazione di quasi-particelle di varia natura in materiali fortemente correlati, che sono al centro dell'attenzione della Fisica della Materia odierna. Essi sono dei composti dalla struttura complessa aventi elementi con shell d o f parzialmente piena, caratterizzati da una preponderante interazione tra gli elettroni che non può essere trascurata nella definizione della struttura elettronica. La RIXS è stata ampiamente utilizzata su ossidi fortemente correlati di metalli di transizione (e dunque con shell d semipiena), e in particolare sui cuprati superconduttori (strutture a strati bidimensionali con piani di CuO_2) per due ragioni.

La prima è il notevole interesse scientifico in superconduttori non convenzionali ad alta temperatura critica: nonostante la ricerca intensiva e molti risultati promettenti, una teoria completa che spieghi la comparsa di superconduttività in materiali non descrivibili con la teoria BCS [3] è ancora assente. Questa attenzione si è rivelata molto stimolante per lo sviluppo della tecnica RIXS, ma ciò non toglie che possa essere fruttuosamente impiegata anche sull'altra classe di materiali fortemente correlati, quelli con shell f semipiena.

La seconda è di carattere tecnico e riguarda la risoluzione in energia. Nel caso dei cuprati, un'eccitazione tipicamente analizzata è l'eccitone lasciato su due diversi livelli $3d$ a seguito di scattering anelastico, noto come eccitazione dd. Energie tipiche sono dell'ordine di $1\ eV$, compatibili con la risoluzione della RIXS da diversi anni. Nel caso di composti di Terre Rare (elementi $4f$), invece, le eccitazioni che in questo caso sono di tipo ff hanno energie ben minori di $1\ eV$, e questo le ha mantenute fino a poco tempo fa solo sul piano speculativo. Ben pochi lavori di RIXS su Terre Rare sono difatti presenti in letteratura (da citare un primo lavoro sul Gadolinio, [4]), e questa Tesi è il primo studio su composti del Cerio.

L'interesse nei materiali basati su Terre Rare risiede nei loro livelli energetici $4f$, che sono fortemente localizzati nel proprio sito atomico ma che allo stesso tempo sono molto vicini al

livello di Fermi, trovandosi quindi coinvolti nelle proprietà di trasporto elettronico.

La struttura elettronica delle Terre Rare determinata dall'accoppiamento Spin-Orbita. Questo, nel caso del Cerio avente un solo elettrone $4f$, produce uno split in soli due stati, ${}^2F_{5/2}$ e ${}^2F_{7/2}$. In aggiunta, l'interazione con il campo elettrico generato dalle cariche circostanti avente la simmetria del cristallo in considerazione e noto come Campo Cristallino (Crystal Field, CF) produce un ulteriore split della degenerazione $2j+1$ di ciascun livello Spin-Orbita, a causa dell'abbassamento di simmetria.

Lo scopo di questa Tesi è analizzare le eccitazioni in cui siano coinvolti due livelli f, note come eccitazioni ff, lasciate nel sistema in seguito a scattering risonante di raggi X soffici. In particolare i due livelli possono avere sia lo stesso momento totale J, sia un J diverso. Nel primo caso si parla di eccitazioni di Campo Cristallino, nel secondo di eccitazioni di Spin-Orbita.

Da recenti misure di spettroscopia di fotoemissione risolta in angolo (ARPES) su un intermetallico di Itterbio [6] è stato provato che l'interazione degli stati $4f$ con le bande di valenza del cristallo, dal carattere tipicamente dispersivo, diventa anch'essa dispersiva, comportando una variazione nella spaziatura e anche nella sequenza dei livelli CF. E' quindi ragionevole aspettarsi che anche le eccitazioni ff presentino un carattere dispersivo. Ricordando la vicinanza al livello di Fermi, questo può avere notevoli e importanti conseguenze nella comprensione generale della Fisica delle Terre Rare.

Abbiamo effettuato le misure su tre diversi campioni. $Nd_{1.84}Ce_{0.16}CuO_4$ è un cuprato ben noto [28], mentre $CeCu_2Si_2$ è il primo superconduttore non convenzionale ad essere stato scoperto [30]; la novità risiede però in entrambi casi nello studio degli elettroni f dell'atomo di Cerio. Il terzo campione, $CeRu_2P_2$, è simile a $CeCu_2Si_2$ in termini di valenza e struttura, e possiede un Campo Cristallino più intenso a causa del maggiore raggio ionico del metallo di transizione.

La simmetria cristallina dei tre campioni è la stessa, tetragonale a corpo centrato. Essi però si differenziano in stato di valenza, come abbiamo dimostrato con misure di assorbimento sull'edge M_5 e M_4. Infatti, tramite un confronto con altri campioni di riferimento, si osserva una valenza di tipo Ce^{4+}, Ce^{3+}, o mista. Da misure di dicroismo lineare si deduce un effetto piccolo del Campo Cristallino, come ci si aspetta data la localizzazione degli elettroni $4f$. Dell'assorbimento, inoltre, sono discusse le differenze tra il segnale di fluorescenza e di elettroni Auger.

Le misure di scattering in risonanza sull'edge M_5 del Cerio permettono di analizzare in dettaglio le eccitazioni ff. $Nd_{1.84}Ce_{0.16}CuO_4$ possiede lo ione Ce^{4+}, dunque una configurazione elettronica $|4f^0\rangle$: non è pertanto possibile avere scattering anelastico che comprenda due diversi elettroni f; coerentemente, abbiamo misurato solamente un picco elastico negli spettri RIXS intorno alle basse energie trasferite. Inoltre si osserva una struttura data dalla fluorescenza, come si può dedurre dalla sua dipendenza lineare dall'energia del fotone incidente. Invece negli altri due campioni $CeCu_2Si_2$ e $CeRu_2P_2$, aventi configurazioni elettroniche rispettivamente $|4f^0\rangle + |4f^1\rangle$ e $|4f^1\rangle$, è presente una struttura inelastica associabile ad una eccitazione di Spin-Orbita. Non si hanno prove evidenti di eccitazioni di Campo Cristallino, e tantomeno una loro possibile dispersione, a causa di mancanza di risoluzione in energia. Tuttavia la larghezza delle strutture negli spettri RIXS molto più grande della risoluzione dello spettrometro costituisce un interessante indizio che può suggerire la presenza di una sottostruttura data dal Campo Cristallino. E' da notare come le nostre misure si trovino in buon accordo con delle simulazioni ottenute da calcoli di multipletto atomici. Infine abbiamo

misurato lo scattering anche dall'edge M_4, dove gli spettri RIXS mostrano gli stessi risultati qualitativi dell'M_5 anche se le intensità delle strutture inelastiche sono molto minori a causa di diverse regole di selezione, e in aggiunta si osservano delle perdite ad alta energia dovute alla conversione Coster-Kronig di tipo MMN.

Nel ***Capitolo 1*** *viene introdotto il caso scientifico e le motivazioni di questo studio.*

Nel ***Capitolo 2*** *verranno presentati i fondamentali delle tecniche di assorbimento e scattering di raggi X, con attenzione rivolta al setup sperimentale e allo spettrometro utilizzato.*

Nel ***Capitolo 3*** *verranno invece descritte le proprietà di valenza e di simmetria dei tre campioni analizzati e la struttura elettronica dell'atomo di Cerio.*

Nel ***Capitolo 4*** *sono quindi mostrati e discussi in dettaglio i risultati delle misure di assorbimento e di scattering, confrontati con le simulazioni.*

Infine nel ***Capitolo 5****, anche alla luce dei risultati ottenuti, verrà mostrato come la RIXS si presenti un promettente metodo di indagine per i materiali $4f$, e ne verrà delineato un possibile sviluppo: la costruzione di un nuovo spettrometro ad alta risoluzione prevista per il prossimo futuro.*

Contents

List of Figures

Chapter 1

Introduction

In the last decades, thanks to the advent of high-brilliance third-generation synchrotron radiation sources and to the evolution of advanced technologies like X-ray optics and photon detectors, a powerful spectroscopy instrument has been developed: the Resonant Inelastic X-Ray Scattering (RIXS). Among its advantages, it is a charge neutral, elemental specific and site selective technique capable to probe energy, momentum and polarization dependence of elementary excitations in complex materials [1].

One of the major interests of experimental and theoretical research in Condensed Matter Physics is the study of *Strongly Correlated Materials* [2]. These systems are compounds having partially unfilled d or f shells elements, whose peculiarity is a strong interaction between electrons that cannot be neglected in the description of their electronic structure. Much of the effort of RIXS works have been put in strongly correlated transition d metal oxides, and in particular superconductive *cuprates* (2D layered structures with planes of CuO_2), for two reasons.

First, the big scientific interest in high-T_c unconventional superconductors: a comprehension of the mechanism for appearance of superconductivity in materials not described by the well known BCS theory [3] is still lacking, despite intensive research and many promising leads. This focus has been beneficial to the development of the technique, but there is a large potential for growth in other fields: for instance, it would be interesting to move on the other class of strongly correlated materials, compounds with partially unfilled f shells.

Second, the actual energy resolution. In the case of cuprates, typical excitations probed by RIXS are the excitons leaved within two different $3d$ levels after X-ray scattering, known as dd excitations. Typical energy are of the order of 1 eV, compatible with the RIXS resolution since several years. On the other hand, in the case of compounds with Rare Earths ($4f$ elements), typical energy of ff excitations are well below 1 eV, making them elusive. There are only few cases in literature of RIXS experiment on Rare Earths (see for example [4]), because of lack of resolution. With recent and incoming resolution upgrades, however, this kind of study is becoming possible.

Electronic and magnetic properties of Rare Earths materials strongly depend on their partially filled $4f$ shells which are so localized deep inside the atomic core that maintain their purely atomic properties; in *Figure 1.1* the $4f$ radial wave function of Ce atom is clearly localized, in opposition with itinerant $6s$ and $6p$ waves. In this case, Spin-Orbit interaction (SO) is the driving force in the building of the electronic structure.

In a Rare Earth material, however, wave functions and energies of ground and excited

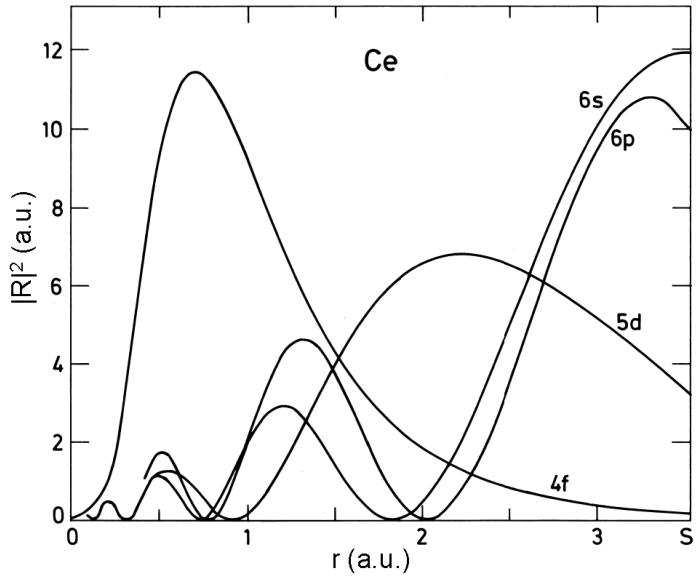

Figure 1.1: Radial wave function $s-$, $p-$, $d-$ and $f-$ type in Ce atom. S is the radius of a sphere of atomic volume [5].

states are actually dependent on the structure and composition of the specific compound, because of the interaction with the non-spherical electrostatic field generated by the ligands, called crystal field (CF), which has to be considered as a perturbation potential. This will cause a fine splitting of each SO splitted levels. In addition, despite their localized nature, $4f$ states could be able to hybridize with valence states thanks to hopping interactions, modifying the charge distribution environment.

In *Figure 1.2* recent Angle Resolved Photo-Emission Spectroscopy (ARPES) measurement on $YbRh_2Si_2$ is shown [6]. It has been proved that since valence states in crystals form dispersing valence bands (1 and 2), the interaction with the $4f$ states (I-IV) becomes dispersive, too, inducing variations in the spacings and in the sequence of the CF energy levels. It is therefore reasonable to suppose to find in RIXS an energy and momentum dependence of *ff* excitations, i.e. excitations between SO and CF splitted $4f$ levels, but these measurements have never been performed before, because of the clear lack of resolution.

It is noteworthy that intermetallics of Rare Earths can show a mixed valence behaviour. This is important because the presence of *ff* excitations depend also on the formal occupation of the levels.

Among Rare Earths, Cerium atom has only one f electron, therefore Spin-Orbit splitting is into only two states. In *Figure 1.3* an unpublished ARPES measure [7] on $CeRh_2Si_2$ is shown. A weak dispersive behaviour of Crystal Field levels and Spin-Orbit splitting is observed. In *Figure 1.4* an Inelastic Neutron Scattering (INS) measure [8] on $CeCu_2Si_2$ is shown. A Crystal Field feature is observed, but the Spin-Orbit energy scale is inaccessible.

In this thesis the results of a study on three Cerium mixed valence intermetallic compounds, $Nd_{1.84}Ce_{0.16}CuO_4$, $CeCu_2Si_2$ and $CeRu_2P_2$, is reported. The aim is to identify and to characterize *ff* excitations and their dispersion, by means of X-ray Absorption Spectroscopy and Resonant Inelastic X-ray Scattering. The experiments were performed at the ID08 beam-

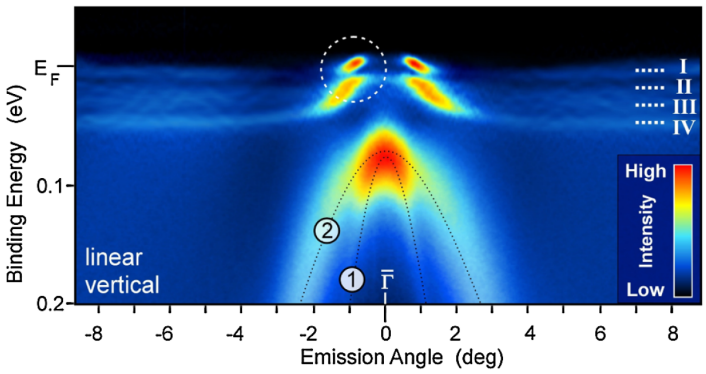

Figure 1.2: ARPES spectrum from the Si-terminated surface of $YbRh_2Si_2$ along the $\bar{\Gamma} - \bar{X}$ direction of the surface Brillouin Zone using 45 eV photons and linear vertical polarization. A bunch of four weakly dispersive states closely below E_F (I-IV) interacts with two hole-like parabolic bands (1 and 2) around the $\bar{\Gamma}$ point. Picture from [6].

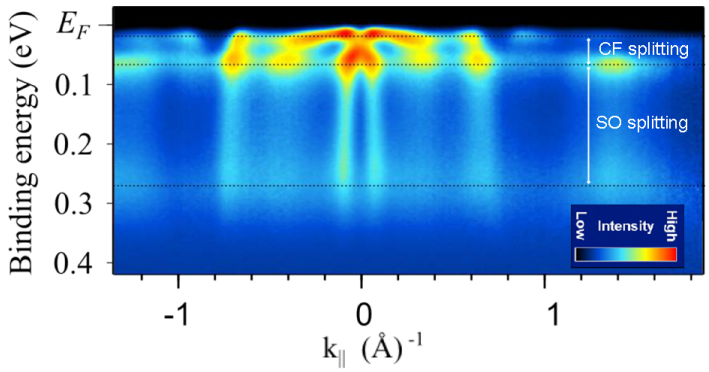

Figure 1.3: ARPES spectrum of $CeRh_2Si_2$. Dispersive Crystal Field levels and Spin-Orbit splitting is observed. Picture from [7].

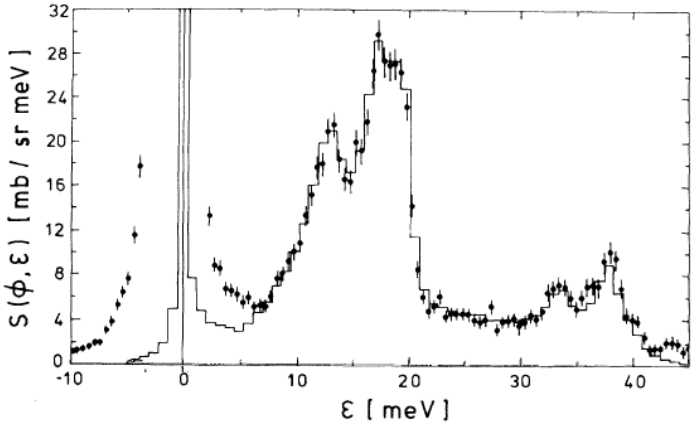

Figure 1.4: Inelastic Neutron Scattering from $CeCu_2Si_2$ measured with an incident energy of 60 meV and scattering angle of 136° (filled circles). The histograms are the total scattering determined by Monte Carlo simulation, not convolved with the instrumental resolution. Picture from [8].

line of European Synchrotron Radiation Facility (ESRF), in Grenoble.

In ***Chapter 2*** fundamentals of X-ray absorption and scattering techniques will be described, with a focus on the experimental setup of the beamline.

In ***Chapter 3*** the electronic structure of Cerium and the valence and symmetry properties of the three samples studied, $Nd_{1.84}Ce_{0.16}CuO_4$, $CeCu_2Si_2$ and $CeRu_2P_2$, are discussed.

In ***Chapter 4*** the results of data analysis will be discussed in detail.

Finally, in ***Chapter 5*** conclusion remarks and possible further developments will be highlighted.

Chapter 2

Experimental techniques

X-ray Absorption Spectroscopy and Resonant Inelastic X-ray Scattering were used to study low energy excitations in Cerium compounds. In the first part of the present chapter a brief description of the underlying theory of the techniques is presented. In the second part the instrumental setup installed at beamline ID08 of the European Synchrotron Radiation Facility (ESRF), where experiments were performed, is described.

2.1 Fundamentals of X-ray absorption and scattering

We refer to X-rays as electromagnetic radiation with energies between 100 eV and 1 MeV. A further distinction is between "soft" and "hard" X-rays, below and above 2 keV respectively. The former interact so much with the matter that they need ultra vacuum technology, while the latter can pass through air and need radiation protection facilities.

Two different families of phenomena can occur when X-ray photons interact with the electrons of a material. In the first one they do not exchange energy, and the interaction is an elastic scattering known as *Thomson scattering*; *diffraction* techniques are based on this, where the quantity of interest is only the momentum exchanged. We are interested in the *spectroscopy* techniques that, on the other hand, are based on momentum *and* energy exchanges: when X-rays of sufficiently high energy interact with a solid they are absorbed, thus core electrons are excited and later relax.

In very general terms, the absorption of radiation of angular frequency ω can be described by the well-known *Lambert-Beer law*:

$$I(\omega) = I_0(\omega)e^{-\alpha(\omega)x} \tag{2.1}$$

where $I(\omega)$ and $I_0(\omega)$ are respectively the transmitted beam intensity and the intensity before the sample, x is the sample length and $\alpha(\omega)$ is the absorption cross-section. This one, from a quantistic point of view, is proportional to the transition probability W_{fi}, that is given by the *Fermi Golden Rule*:

$$W_{fi} = \frac{2\pi}{\hbar} \left|\langle\psi_f|T|\psi_i\rangle\right|^2 \delta(E_f - E_i - \hbar\omega) \tag{2.2}$$

where the ψ are the wave functions and the E are the eigenvalues, with f and i referring to the *final* and the *initial* state; the δ function account for the energy conservation, the squared matrix element gives the transition rate and the transition operator T contains all

the possible transitions. This can be separated into different orders $T = T_1 + T_2 + ...$, where the operator T_1 stands for the one-photon transitions, T_2 for the two-photons transitions, and so on [9].

The interaction Hamiltonian of the system H_{int}, being $H_{total} = H_0 + H_{rad} + H_{int}$ where H_0 is the unperturbed Hamiltonian and H_{rad} describes the (plane) electromagnetic wave, can be separated in different terms as well as T, thanks to a perturbation approach. The two operators T and H_{int} are related by means of the *Lippmann-Schwinger equation*:

$$T = H_{int} + H_{int}\frac{1}{E_i - H_0 + i\Gamma/2}T \tag{2.3}$$

where Γ is the lifetime broadening of the excited state. This can be solved by iteration, giving at first order $T_1 = H_{int_1}$ [10]. This is useful in order to describe single-photon transitions, such as X-ray absorption or emission. X-ray scattering is a two-photons process, because it is describable as the (virtual) absorption into an intermediate state and the subsequent decay with emission of a new photon: in scattering theories the second order solution has to be considered.

Among the various X-ray spectroscopy techniques we performed Near Edge X-ray Absorption Fine Structure (NEXAFS) and Resonant Inelastic X-ray Scattering (RIXS), both possible with the use of *synchrotron radiation* (see *Section 2.2.1*).

2.1.1 X-ray Absorption Spectroscopy

X-ray Absorption Spectroscopy (XAS) is a class of techniques based on the measurement of a signal proportional to the absorption cross-section. Scanning with increasing incident photon energy the trend of $\alpha(\omega)$ is monotonically decreasing because of the atomic cross-section in this energy range, according to the empirical *Pierce-Bragg relation*:

$$\sigma_{photoelectric} = \alpha/\rho \propto E^{-(2.5 \div 3)} \tag{2.4}$$

being ρ the density of the sample [11]. When the photon energy, though, equals the binding energy of a core electron, it is absorbed, and so $\alpha(\omega)$ increases abruptly, in a step that is commonly called 'edge', and then it starts to decrease again (see *Figure 2.1*). For labeling the edges it is traditionally used the *Siegbahn notation*, common in X-ray science: given a transition from an atomic level (n l j) to the continuum, it is named K,L,M,... for increasing n, with sequential numbers for increasing (l,j) (e.g. $3d_{5/2}$ is labeled M_5).

For different atoms the binding energy of a given core shell is different, because of different nuclear charge attraction, higher for heavier atoms: for this reason XAS techniques are *elemental selective*. It means that the same edge will be right shifted for increasing atomic number, as it is shown in *Figure 2.1* for the M and L edges in La and Ce (note that L_3, L_2, L_1 edges are visible).

In *Figure 2.2* a simple picture of the absorption process is shown. In this case X-ray photons of different energies interact with a $3d_{5/2}$ core electron. Up to the Fermi level E_F there are no available levels where the electron can go, so the photons with this energies are not absorbed by the considered core level. On the other hand, above the vacuum energy E_{vac} the electron can reach a plane wave continuum state with increasing kinetic energy, and the absorption edge appears. Finally, when the energy is between E_F and E_{vac} the core electron can reach empty valence levels: this gives rise to resonances in the absorption that can be also very intense.

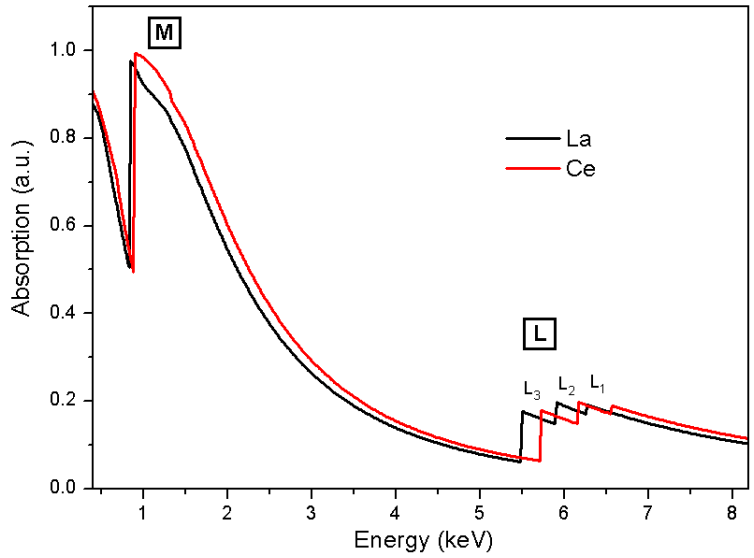

Figure 2.1: M and L edges in La and Ce, 0.5 μm thickness. The more bound the core electron is ($n = 3, 2$) the more energy is required to extract it. The position in energy of the edge increases with the atomic number. Picture from [12].

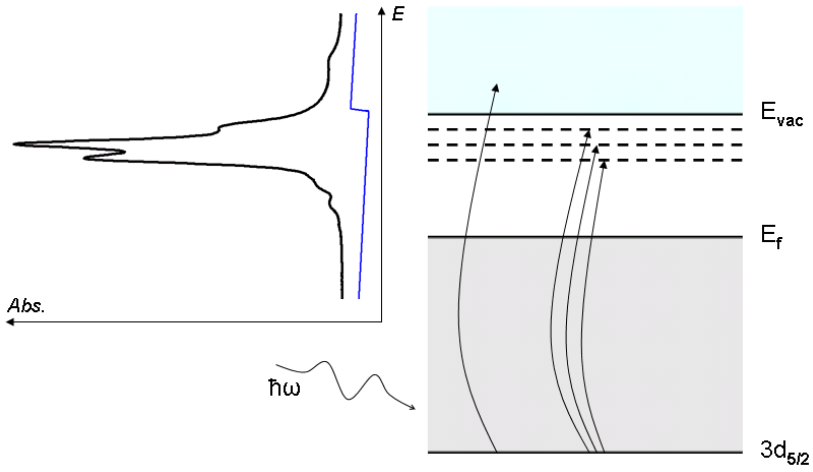

Figure 2.2: Picture of the absorption process.

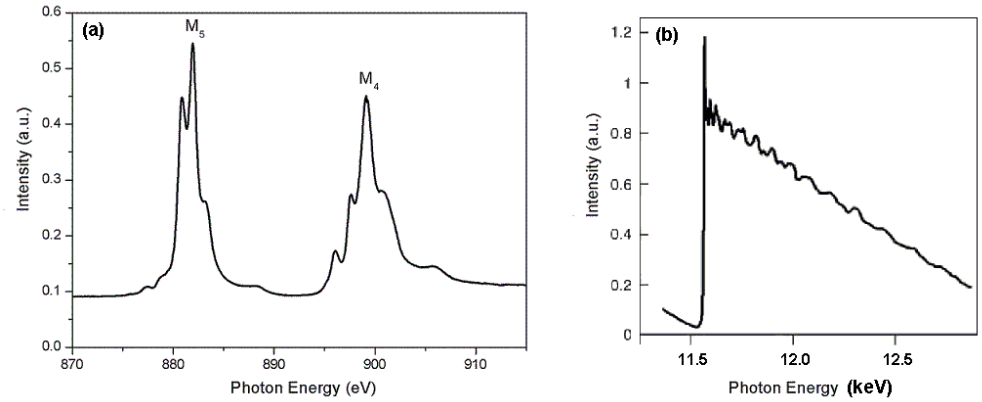

Figure 2.3: Examples of XAS spectra. *Panel (a)*: NEXAFS M_5 and M_4 edges of cerium in $CeCu_2Si_2$ (measurement performed at ID08, ESRF). *Panel (b)*: EXAFS L_3 edge of metal Pt (from [10]).

Figure 2.3(a) shows a typical XAS spectrum. Two structured features clearly arise in correspondence of the M_5 and M_4 edges, coming from the resonance levels. In this case they are predominant respect to the height of the step. When the energy range continuously spanned is smaller than 100 eV the technique is also known as Near-Edge X-ray Absorption Fine Structure (NEXAFS). On the other hand, if the energy range is much bigger the XAS is also called Extended X-ray Absorption Fine Structure (EXAFS). In this case the analysis focuses on to the oscillations occurring far from the edge (see *Figure 2.3(b)*). They can give information about atomic pair interdistance distribution, because they arise from interference processes between the incident light and that backscattered from the environment of the absorber atom. The contribution to the interference due to multiple scattering events increases in NEXAFS, because the photon energy is sufficiently near to the edge [13]. For this reason, whereas in EXAFS is possible to obtain an analytical description of a spectrum, the analysis of NEXAFS data is typically made by comparison with simulated spectra.

It is noteworthy that XAS do not require long range ordering in the sample, because its information, topological and chemical, come from the nearest neighbours of the atom considered; nevertheless, it is not a local technique, such as scanning probe microscopies, but the detected signal is a spatial average over a certain area of the sample determined by the beam spot size.

NEXAFS is a good technique for deducting oxidation state of the sample in a non destructive way. This is particularly interesting when studying samples with mixed valence: the more an atom is oxidized the more its absorption edge is shifted to higher energy, and the spatial average of different contributions with certain weight contemporaneously present in the sample will give rise to structured features (see *Figure 2.4*). The shifting occurs because in an oxidized atom the shielding of the nuclear charge due to the electron cloud is reduced; therefore the more the oxidization is the more bound a core electron is, meaning that it requires more energy to be excited.

Before the resonances is possible to observe structures called pre-peaks: they are due to transition into states forbidden by selection rules that are hybridized with permitted ones; in addition, many multiple events, such as shake-up and shake-down electron transitions, can occur (for details, see [14]).

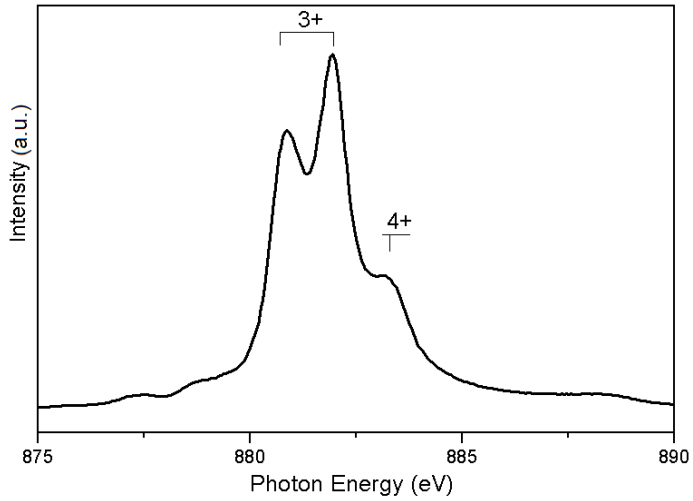

Figure 2.4: Mixed valence effect on M_5 Ce absorption edge in $CeCu_2Si_2$. The whole peak is the sum of two contributions from 3+ and 4+ Ce atoms (measurement performed at ID08, ESRF).

Since the core electron state is well-known, another important information provided by XAS spectra is the symmetry of the final excited state, that depends on the symmetry of the initial core state, on the polarization of the incident X-ray and on the selection rules of the considered transition. Because absorption is a single-photon interaction, $T_1 = H_{int_1}$ as shown before. The X-ray wave is usefully described by the vector potential considered as a quantum mechanical operator, in the frame of the second quantization model:

$$\mathbf{A}(\mathbf{r}) = \sum_{\mathbf{k},\lambda} A_0(k)\mathbf{e}_{\mathbf{k},\lambda}(b_{\mathbf{k},\lambda}e^{i\mathbf{kr}} + b^{\dagger}_{\mathbf{k},\lambda}e^{-i\mathbf{kr}}) \tag{2.5}$$

where λ is the polarization, $b^{\dagger}_{\mathbf{k},\lambda}$ and $b_{\mathbf{k},\lambda}$ are creation and annihilation operators fulfilling the commutation relation of bosons, $\mathbf{k}$ is the wavevector, $A_0(k)$ is a normalization constant and $\mathbf{e}_{\mathbf{k},\lambda}$ is the potential vector's versor.

From well-known perturbation theory and under Coulomb gauge is possible to explicitly calculate H_{int_1} [10]:

$$H_{int_1} = \frac{e}{mc}\sum_i \mathbf{p}_i \cdot \mathbf{A}(\mathbf{r}_i) + \frac{e}{2mc}\sum_i \sigma_i \cdot \nabla \times \mathbf{A}(\mathbf{r}_i) \tag{2.6}$$

where $\mathbf{p}_i$ is the momentum and σ_i the spin of the i electron. The second term describes the spin interaction, that being a relativistic effect is neglectable. Using (2.5) in (2.6), being $T_1 = H_{int_1}$ and expanding with Taylor until the second order we obtain, for each electron:

$$T_1 = \sum_{\mathbf{k},\lambda} b_{\mathbf{k},\lambda}\frac{e}{mc}A_0\left[(\mathbf{e}_{\mathbf{k},\lambda}\cdot\mathbf{p}) + i(\mathbf{e}_{\mathbf{k},\lambda}\cdot\mathbf{p})(\mathbf{k}\cdot\mathbf{r})\right] \tag{2.7}$$

that describes the electric dipole and quadrupole transitions. In soft X-rays $\mathbf{k}\cdot\mathbf{r} < 10^{-2}$, and so with a good approximation only the first term can be considered. Note that $\mathbf{k}\cdot\mathbf{r} \ll 1$ means to consider $\mathbf{A}(\mathbf{r})$ constant, that is true when the wavelength of the X-ray is much bigger than the electron shell considered. This is known as *dipole approximation.*

Now it is possible to substitute T_1 in (2.2) using the Heisenberg equation $[r, H] = \frac{i\hbar}{m}\mathbf{p}$, but before is better to make an other important assumption: the *single-electron approximation*. If all the other electrons in the atom and in the surroundings do not participate in the X-ray induced transition process, then is simple to write the initial state as a well-known core wave function (c), and the final state as a free electron wave function (ϵ) with a core hole ($\underline{c}$). So we obtain for the square matrix element M^2:

$$M^2 = |\langle\psi_f|\mathbf{e_k}\cdot\mathbf{r}|\psi_i\rangle|^2 = |\langle\underline{c}\epsilon|\mathbf{e_k}\cdot\mathbf{r}|c\rangle|^2 \tag{2.8}$$

The transition probability W_{fi} is thus nonzero only if (i) the spin is conserved, $\Delta S = 0$, because the X-rays do not carry spin, and if (ii) the orbital quantum number of the final state differs by 1 from the one of the initial state, $\Delta L = \pm 1$, because of the change of parity with the $\mathbf{r}$ operator. These are the *dipole selection rule*. When considering also the quadrupole transition, the (ii) becomes $\Delta L = \pm 2$.

Multiplet approach

Given a certain electron configuration, there are several possible levels of increasing energy to be considered. These go under the name of *multiplet structure* [15]. Then in the ground state of the system only the thermally accessible levels will be populated.

For example, when considering a Rare Earth atom no more isolated but located in a solid, the atomic levels are influenced by the surroundings depending on the symmetry of the system. A useful model used in the description of the surroundings is the *Crystal Field Theory*, or Ligand Field Theory, where the Hamiltonian of the considered atom includes a perturbation potential term coming from the electrostatic field generated by the charges in the environment. This potential is written as a series expansion of spherical harmonics. It is therefore possible to perform perturbation calculations, with several parameters describing the matrix element of the perturbation potential. Varying these parameters is possible to reproduce, for instance, the experimental absorption spectra. In this case changes of the multiplets in the final state of the absorption process due to the overlap of the core hole wave function with the partially filled valence levels have to be considered.

A further improvement consists in the addition of several corrections coming from the so-called *charge transfer effect*, i.e. the electric field is not treated as a static field, but accounts also for possible charge hoppings between different sites.

Detection

There are several ways to detect the XAS signal, depending on different physical processes and on the particular experimental setup. The most direct, for example, is to measure with ionization chambers the intensity of the incident beam and that of the transmitted one, according to (2.1). Another way is to probe the various channels of decay of the core hole created with the absorption process, as shown in *Figure 2.5*: the fluorescence decay (*2.5(a)*) and the Auger effect (*2.5(b)*).

The fluorescence yield (FY) is not simply proportional to the absorption cross-section, because being a radiative transition dipole selection rules must be considered. The more photons are absorbed, the more core hole are created, and so the more fluorescent X-ray photon are emitted; nevertheless, in $3d$ metals at the L edge and in RE at the M edge the FY can vary drastically, depending on the symmetry of the final state [10]. The mean free

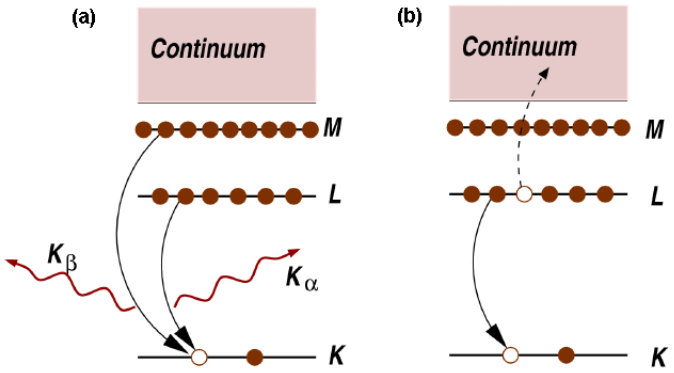

Figure 2.5: Detection of the absorption process. *Panel (a)*: fluorescence emission from different core levels. *Panel (b)*: Auger electron (for details see [13]).

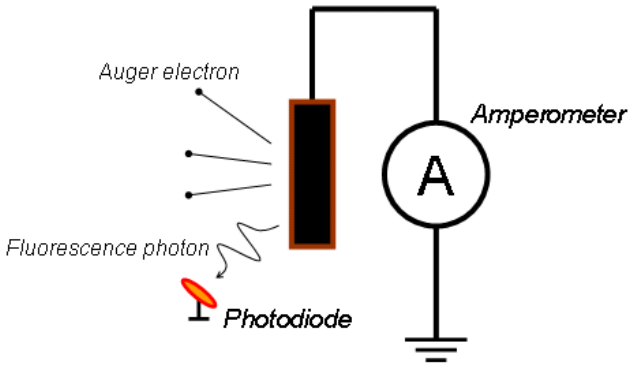

Figure 2.6: Measure of Absorption signal. A photodiode measures the FY from the fluorescence photons emitted, and an amperometer in a circuit with the sample holder measures the TEY from the current due to the leaving of Auger electrons.

path of the fluorescent photon is of the same order of the incident one, and so surface effects are reduced; this however entails self-absorption and saturation effects (see *Section 4.1.1*).

The total electron yield (TEY) is the counting of all the electrons emitted by the sample, independent of their energy. In this case radiative transitions are not involved and therefore there are no selection rules: for this reason TEY is more related to the absorption than FY. The measurement can be a direct count with an electron multiplier of the electrons coming out from the surface. An other way is to measure the drain current that flows in order to maintain charge neutrality, when the sample holder is placed in a circuit. In any case, TEY is a surface sensitive measure, because the electron mean free path is about 10 nm.

Both the fluorescence photons and Auger electrons can be selected in a small energy range, thus removing the lifetime broadening of intermediate states. In this case we talk of partial FY and partial EY [10].

In *Figure 2.6* a scheme of XAS measurements setup is shown. After the absorption of X-rays, Auger electrons and X-ray photons are emitted, counted by an amperometer and a photodiode respectively.

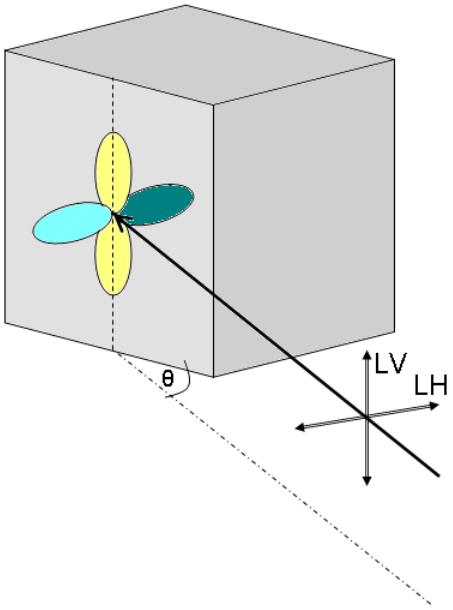

Figure 2.7: Orbitals probed by different polarizations, LV or LH, of an incident beam at θ.

X-ray Linear Dichroism

Thanks to the polarization of the incident X-rays well selectable in a synchrotron light source (see *Section 2.2.1*), it is possible to obtain information about the spatial orientation of the orbitals with respect to the incoming electric field vector **E**. The analysis of differences in spectra obtained with two different linear polarizations, such as LH and LV (horizontal and vertical respect to the synchrotron plane), goes under the name of X-ray Linear Dichroism (XLD).

A geometric dipole selection rule requires that the dipole must have a component in the direction of **E**. In particular, the intensity of the resonance associated with a specific orbital final state is largest if **E** points in the direction of that orbital, and vanishes if **E** is perpendicular [16]. As example let us consider *Figure 2.7*, with a sample made of p-type orbitals. If the light has LV polarization the electric field is always in plane, meaning that it will excite dipole in that direction: yellow orbital will be probed, pale blue will not; note that if the orbital was rotated by 90° in the surface plane (not drawn in the picture) it would not be probed. On the other hand, with LH polarization the electric field will excite a dipole of the pale blue orbital, whereas will not interact with the yellow one; note that in this case the electric field has a component also in the surface plane, so that it can probe the rotated orbital considered before.

2.1.2 Resonant Inelastic X-ray Scattering

X-ray scattering is a two-photons process: a photon-in is absorbed by a core electron, that jump into an intermediate level $|i\rangle$, and the subsequent decay of this excitation gives a photon-out; the final state $|j\rangle$ can in principle be different from the initial ground state $|g\rangle$, and in this case the scattering is inelastic. Among the X-ray Emission Spectroscopies (XES), the Resonant Inelastic X-ray Scattering (RIXS) consists in the use of incident photons with energy

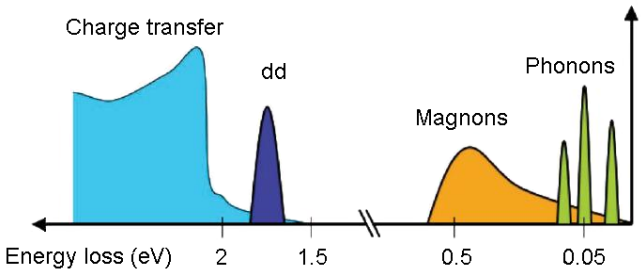

Figure 2.8: Different elementary excitations probed by RIXS and their energy scales in strongly correlated electron materials [1].

resonant to the absorption threshold, evaluated with a preliminary XAS, and in the detection of the energy losses due to inelastic processes.

Because of the participation of an intermediate level in scattering, equation (2.2) is no longer valid, and the correct description of such a two-steps mechanism is made by a second order perturbation development of (2.3). The double-differential cross-section respect to solid angle and energy $d^2\sigma/[d\Omega\, d(\hbar\omega_{out})]$ of the coherent second order process is expressed by the *Kramers-Heisenberg formula* (for details, see [17] and [1]). Its essential part when considering the RIXS case, i.e. with $\hbar\omega_{in}$ close to the core electron excitation threshold, can be expressed as:

$$\frac{d^2\sigma}{d\Omega\, d(\hbar\omega_{out})} \propto \sum_j \left| \sum_i \frac{\langle j|T|i\rangle \langle i|T|g\rangle}{E_g + \hbar\omega_{in} - E_i - i\Gamma_i} \right|^2 \delta(E_g + \hbar\omega_{in} - E_j - \hbar\omega_{out}) \qquad (2.9)$$

where T is the radiative transition and Γ_i is the broadening of the intermediate state ($\Gamma_i = \hbar/\tau_i$, being τ_i the core hole lifetime).

Because of the square module in (2.9), the sum over the various intermediate state cannot be separated into different independent transitions, absorption and emission, but they have to be considered together as a coherent process. When a set of degenerate intermediate states, that are *not* observed, are present, the amplitude must be squared only *after* having superimposed all the states taking into account also the relative phases, as usual in quantum mechanics. It is interesting that two consecutive dipole transitions provide the possibility to move from $|g\rangle$ to $|j\rangle$ even when the direct transition is forbidden by selection rules.

The δ Dirac in (2.9) assures the energy conservation, stating that the difference in photon energies equals the excitation energy of the system. Therefore any spectral peak due to a well defined excitation of the sample with non dispersing behaviour is found at constant transferred energy. The elementary excitations of a material determine many of its physical properties, such as transport properties and its response to external perturbations. Strongly Correlated Materials are of special interest in actual condensed matter Physics, because the low-energy electronic properties are strongly influenced by electron-electron interactions [1].

A big family of solid excitations, usually considered as quasi-particle, can be probed with RIXS. Among these we can identify with increasing transferred energy, as shown in *Figure 2.8*, phonons, magnetic excitations, orbital excitations, charge transfers. *Phonons* correspond to lattice vibration bosonic modes of a periodic solid, with energies typically below 0.1 eV, so that their detection is only just possible with present day RIXS resolution [18].

When magnetic order sets in, the global spin rotation symmetry in the material is broken,

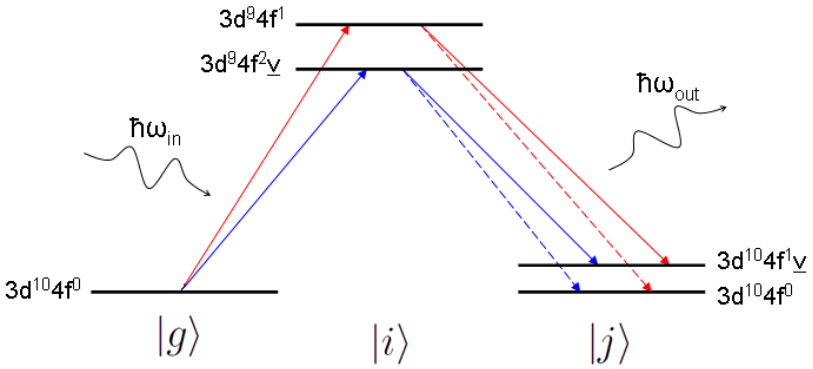

Figure 2.9: Energy level diagram of resonant $3d \rightarrow 4f \rightarrow 3d$ transitions for Ce^{4+}. Two different absorption resonances are shown in blue and red. Dashed lines represent the elastic scattering.

causing collective magnetic excitations, associated to *magnons* and to interactions between them, *bimagnons*. Magnon energies can extend up to 0.3 eV, e.g. in cuprates, and recently magnon dispersions have been measured for the first time with X-rays at the Cu L edge on thin films of La_2CuO_4 [19].

Valence electrons can occupy different sets of orbitals in many strongly correlated systems. Excitations can occur from the orbital ground state, determined by single-ion considerations, to different orbital splitted levels; transitions between different d orbitals are called *dd excitations*.

Charge transport in solids is determined by the energetics of moving electrons from one site to another. Excitations across the optical gap are *charge-transfer* excitations, due to an electron hopping from a ligand site to a metal site [20].

In order to explain the RIXS mechanism let us consider the energy level diagram in *Figure 2.9*. In this example CeO_2 (with Ce^{4+}) M_5 absorption edge is considered (for more details see [21]). The $|g\rangle$ state is in this case $3d^{10}4f^0$. The $|i\rangle$ state is a combination of $3d^9 4f^2 \underline{v}$ and $3d^9 4f^1$, being $\underline{v}$ a hole in the valence band. In fact in this case is possible to have a charge transfer from the valence band to the Cerium atomic f shell. This two levels correspond to two peaks in a XAS measurement, from which one can choose the incident photon energy, blue or red path in the picture, to perform RIXS. If the final state $|j\rangle$ is again $3d^{10}4f^0$ configuration, the scattering is elastic (dashed lines), i.e. $\hbar\omega_{out} = \hbar\omega_{in}$. On the other hand, if the $|j\rangle$ state is higher than the ground state, in this case $3d^{10}4f^1\underline{v}$ configuration, the scattering is inelastic, with $\hbar\omega_{out} < \hbar\omega_{in}$. In this case a Charge Transfer excitation is left into the system, with energy $\hbar\omega_{in} - \hbar\omega_{out}$.

Because of its photon-in/photon-out nature, RIXS is a neutral process, avoiding many charging problems that are typical of other energy loss techniques, such as Electron Energy Loss Spectroscopy. In addition, it probes bulk properties thanks to the penetration of photons, but can be performed also in surface, using grazing incidence or thin samples. Because of the resonance chosen with XAS, RIXS is *elemental specific*, and because of the localization of core electrons involved in the transitions it is also *site-selective*. Varying the angles in the geometrical setup is possible to scan different momentum-transfers, thus measuring dispersion of excitations. It is clear that RIXS gives much more information than the only XAS, but

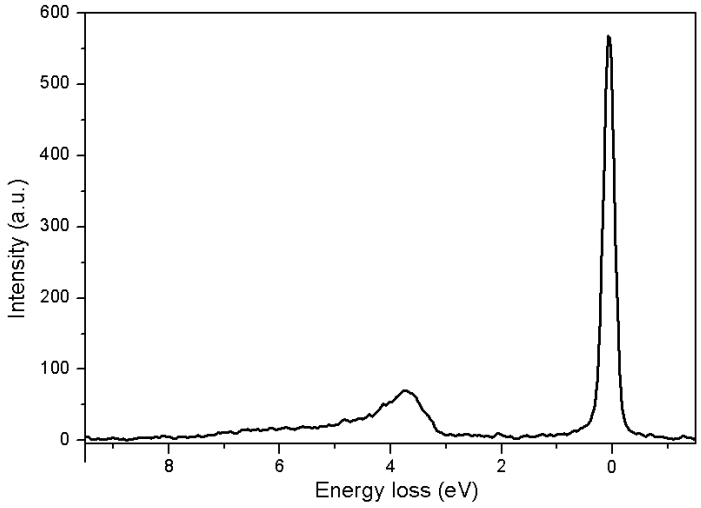

Figure 2.10: Example of RIXS spectrum: NCCO sample, photon energy 883.7 eV (measurement performed at ID08, ESRF).

the signal intensity is drastically lower being a second order process; it means that it is a photon-hungry technique, so that the use of high-brilliance x-ray sources (see *Section 2.2.1*) is unavoidable, as well as the need of highly efficient detectors (see *Section 2.2.3*).

In *Figure 2.10* is shown an example of RIXS spectrum. In the abscissa there are the energy losses: at 0 eV the elastic Thomson scattering contributes with a peak that, in general, has got a Voigt profile: a Lorentzian intrinsic lineshape convolved with the Gaussian profile with FWHM given by the spectrometer resolution. On the left, at different energies, several features can arise, due to different energy losses transferred to the system.

2.2 Instrumentation

Our experiments were conducted at the ID08 beamline of European Synchrotron Radiation Facility (ESRF), in Grenoble. In this section the experimental setup will be shown: in the first part synchrotron radiation properties are briefly described, then a simple scheme of the whole beamline is shown, and finally a major attention will be dedicated to the RIXS spectrometer.

2.2.1 Synchrotron radiation

When charged particles are forced by electric and magnetic fields to follow circular trajectories at relativistic speed, they emit electromagnetic radiation in a narrow cone in the direction of their motion; this is called *synchrotron radiation* (for details see [22]). The first observation came at General Electric in 1947: in the beginning it was considered as a problem, being the major energy loss term for particles in accelerators, but after twenty years the first facilities dedicated to synchrotron radiation production were made, because of its very peculiar properties that are so useful in the study of matter Physics [23]:

- The spectral range of synchrotron radiation is very broad and continuous, and varies from the IR up to the hard X-ray, because of a combination of relativistic Doppler effect

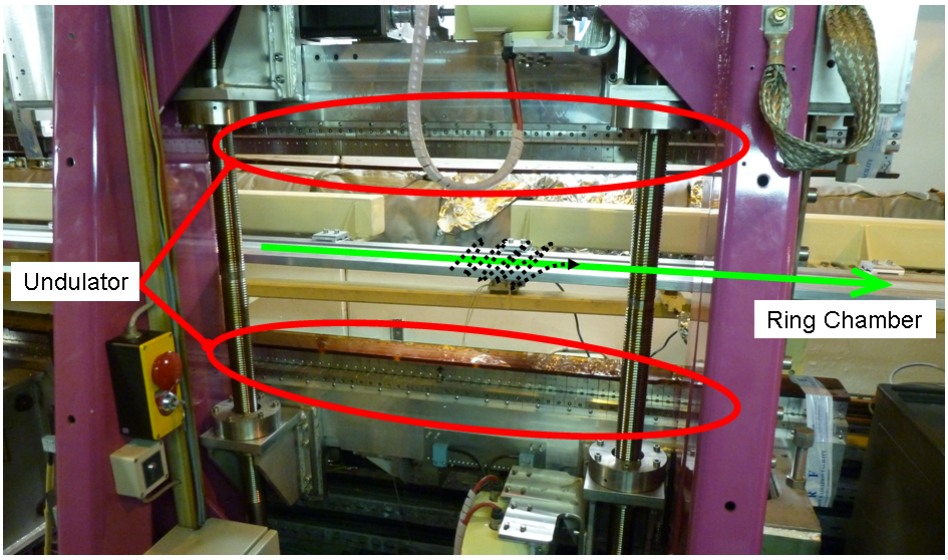

Figure 2.11: An Insertion Device installed along the ring of ESRF. The undulator made of an upper and a lower series of permanent magnets is shown. When the electron beam in the ring chamber passes through the ID, the electrons oscillate emitting synchrotron radiation. This have properties dependent on the magnets pattern.

and time contraction. The central frequency depends both on the emitting particle energy and on the strength of the magnetic field, and so it is tunable with continuity.

- The beam presents very high intensity, is well collimated and has a pulsed time structure.
- The source has extraordinary high brilliance, that is an invariant quantity in the phase space. This is made by constructing very low emittance machines, i.e. minimizing the source size and the beam divergence. High brilliance allows very large sensitivity in spectroscopy.
- The polarization, both linear and circular, can be controlled, acting opportunely on the devices that bend the electrons.

In *Figure 2.11* an undulator installed in the ESRF storage ring is shown. It is a kind of insertion device (ID), so called because it is put in the linear path between two bending magnets (BM). Whereas the latter are made by a single big dipole magnet and its main characteristic is the stability, the former is made by a periodic sequence of small dipole magnets and is focused on optimizing the brilliance.

2.2.2 The beamline

ID08 beamline is an intense source of polarized soft X-rays that is principally used to probe electronic structure and magnetism in a diverse range of systems with X-ray absorption and scattering. The beamline is equipped with:

- two APPLE II undulators providing circular or linear polarization

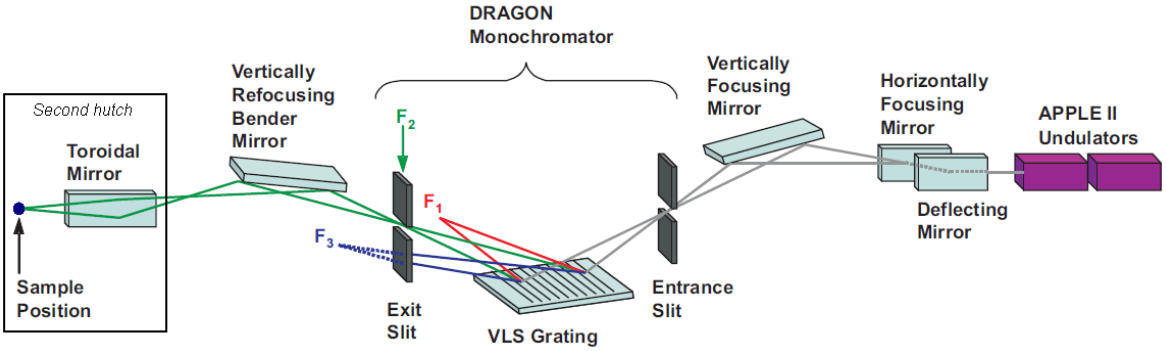

Figure 2.12: Sketch of the ID08 beamline at ESRF. For details see the text and [24].

- a spherical grating monochromator Dragon type [25] with an energy resolution close to $E/\delta E = 5000$ at 930 eV
- optics focusing down to $6 \div 40$ μm (FWHM) in the vertical beam size, and $60 \div 500$ μm in the horizontal
- several different UHV experimental stations and sample preparation facilities

In *Figure 2.12* a simple sketch of ID08 is shown. The flux of the radiation emitted by the undulators at 1 keV is $1.4 \cdot 10^{15}$ ph/s/0.1%BW (photons per second per relative spectral bandwidth of 10^{-3}) at the maximum ring-current of 200 mA. The beam is deflected and shaped by a series of optical elements based on grazing incidence mirrors.

Then the beam enters in the Dragon monochromator, composed of an entrance slit, a dispersive optical element and an exit slit. The entrance slit aperture defines the position of the source seen by the grating. This is a variable line spacing (VLS) grating (1200 lines/mm) with fixed radius of curvature (57.3 m), that disperses photons with different energies, tunable in the range $0.3 \div 1.6$ keV, making it ideal for studying the magnetic and electronic properties of transition metals and rare earths. The exit slit spatially filters the diffracted beam and defines the energy resolution of the beamline: the narrower the slits are, the better energy resolution is obtained, though having a cost in reduction of the flux.

Downstream the monochromator the absorption of a reference sample can be measured. In our particular setup a CeF_3 cell was installed. Finally the beam is sent in one of the two hutches of the beamline, where first of all it is refocused and its intensity I_0 is measured. In the first hutch a high field magnet (HFM) for absorption and X-ray Magnetic Circular Dichroism (XMCD) measurements is installed, whereas the RIXS setup is located in the second one.

The beam size at the sample in the RIXS hutch is 50×8 μm^2. A CCD camera images the visible light generated by the X-rays on a YAG screen located at the bottom of the sample holder in order to determine the spot size in the horizontal direction. The more accurate measure of the vertical spot width is made by a razor blade, that is mounted below the YAG screen (see *Figure 3.1*) and scanned in the vertical direction in steps of 0.5 μm. Measuring the drain current flowing through the sample holder during the vertical scan the profile of the blade itself is obtained. Thus the FWHM of its derivative is a direct measure of the vertical beam spot. The best FWHM achieved is around 5 μm.

The sample holder is located in a UHV chamber on a manipulator which can move in the three x, y, z directions and can rotate in the z axis by the angle δ (see *Figure 2.13*). Here

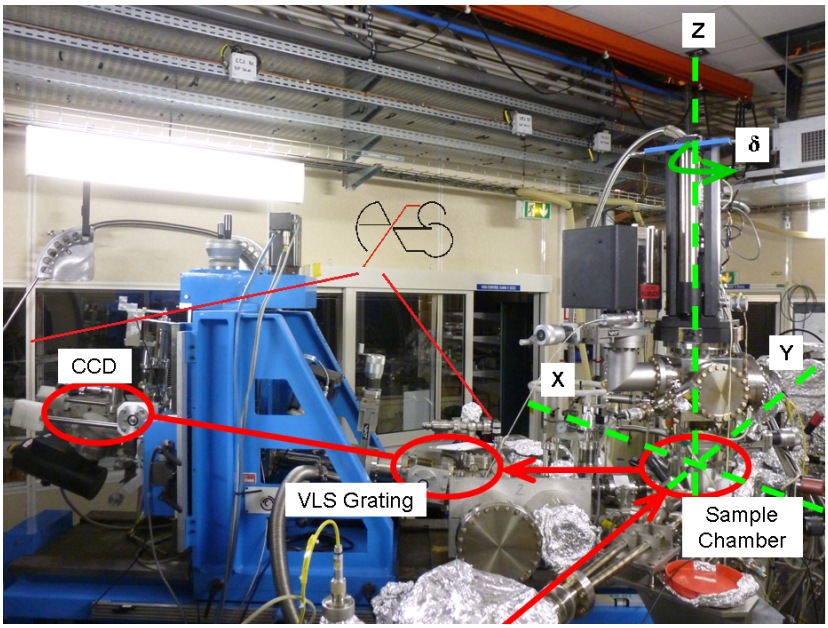

Figure 2.13: The RIXS experimental hutch at ID08, ESRF. The sample chamber with the coordinate system and the AXES spectrometer are indicated.

a photodiode and a dedicated circuit measure the FY and the TEY respectively (see also *Figure 2.6*), and in addition the temperature is measured, because it can change down to few Kelvin thanks to a Helium flow cryostat.

At a fixed angle of 50° from the incident beam the scattered photons are brought to the AXES spectrometer (Advanced X-ray Emission Spectrograph [26]).

2.2.3 Advanced X-ray Emission Spectrograph

The spectrometer consists in a VLS grating and a charge coupled device (CCD) detector, cooled by liquid nitrogen in order to reduce the thermal noise. The entrance and exit arms are long 0.6 m and 1.6 m respectively; the total length of the spectrometer (L) and the horizontal dimension of the detector (D) determine the angular acceptance of the instrument proportional to D/L.

The grating has an average density of 2400 lines/mm and its aim is both to spatially separate different energy components of the beam by diffraction and to focus them onto the detector, so that the vertical position of a photon counted is in direct correspondence with its energy because of the *grating equation*:

$$d(\sin\alpha - \sin\beta) = n\lambda \tag{2.10}$$

where d is the line spacing, α and β are the incidence and exit angle respectively (referred to the grating normal), λ is the light wavelength and n is an integer.

It is possible to work in entrance slit-less conditions because the light spot on the sample in the vertical direction $s \approx 5$ μm is quite small, and can act as the source of the spectrometer itself. The virtual exit slit is instead determined by the spatial resolution of the CCD detector. Each photon which hits the wafer causes the release of a charge cloud onto a number

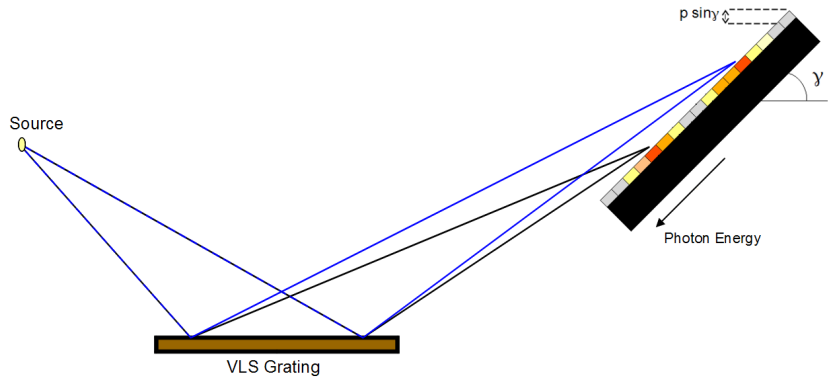

Figure 2.14: Scheme of the spectrometer. The VLS grating spatially disperse different energies of photons that impinge on the CCD detector, mounted at grazing incidence.

of neighbouring pixels as a consequence of split event [27]. Therefore the effective spatial resolution of modern CCD (p) is around 25 μm, independent of the pixel size. In order to improve the resolution the CCD is thus mounted at grazing incidence at angle $\gamma \sim 20°$, so that the effective exit slit becomes $p \cdot \sin(\gamma)$ (see *Figure 2.14*), becoming comparable to s.

In *Figure 2.15* is shown a raw image on the detector. Because of (2.10) photons with increasing energies are distributed from the bottom to the top on the CCD, as shown in *Figure 2.14*. Therefore summing over the horizontal direction the RIXS spectrum can be extracted just as an histogram. The shape of a certain photon energy is not actually a straight line onto the CCD, but it is a sort of arc: this come from focusing properties of the spherical (and not plane) grating, and it is corrected by software with parabolic interpolation.

Increasing statistics requires increasing counting time, and being RIXS a second order photon-hungry technique it takes usually from 30 to 120 minutes for each spectrum. In order to avoid possible drifts of the optics, with subsequent loss in resolution, every single spectrum like that of *Figure 2.15* is generated as the sum of many 5 minutes long acquisitions.

It is noteworthy that in the actual setup the CCD is rotated along its normal axis. If a certain row of the CCD does not work properly a very sharp artifact will affect the spectrum, but if the CCD is rotated this artifact will be spread onto different energies.

In order to assign the proper energy scale to the spectra, that are discretized in pixels, before the experiments a calibration procedure is performed. This consists in evaluating the slope of the incoming photon energy, increased step by step by 0.5 eV, versus the elastic peak position measured in pixel (see *Figure 2.16*).

A critical feature of the spectra extracted is the effective exact position of the zero energy loss, i.e. of the elastic peak. This is important both when summing a set of 5 minutes long spectra, and when it is interesting to have a comparison between different situations, such as different incidence angle or photon energy: in both cases the spectra have to be well aligned to their zeros. Therefore in order to have a reference a piece of carbon tape is fixed close to each sample, as can be noticed in *Figure 3.1* . Before every set of acquisitions on samples a spectrum onto the carbon tape is measured. The photon energy is very far from the absorption edge of the carbon atom, and so the spectrum is considered completely elastic. This is useful also in order to evaluate the actual resolution, by measuring the FWHM of this peak. *Figure 2.17* shows a NCCO sample spectrum aligned with its carbon tape reference.

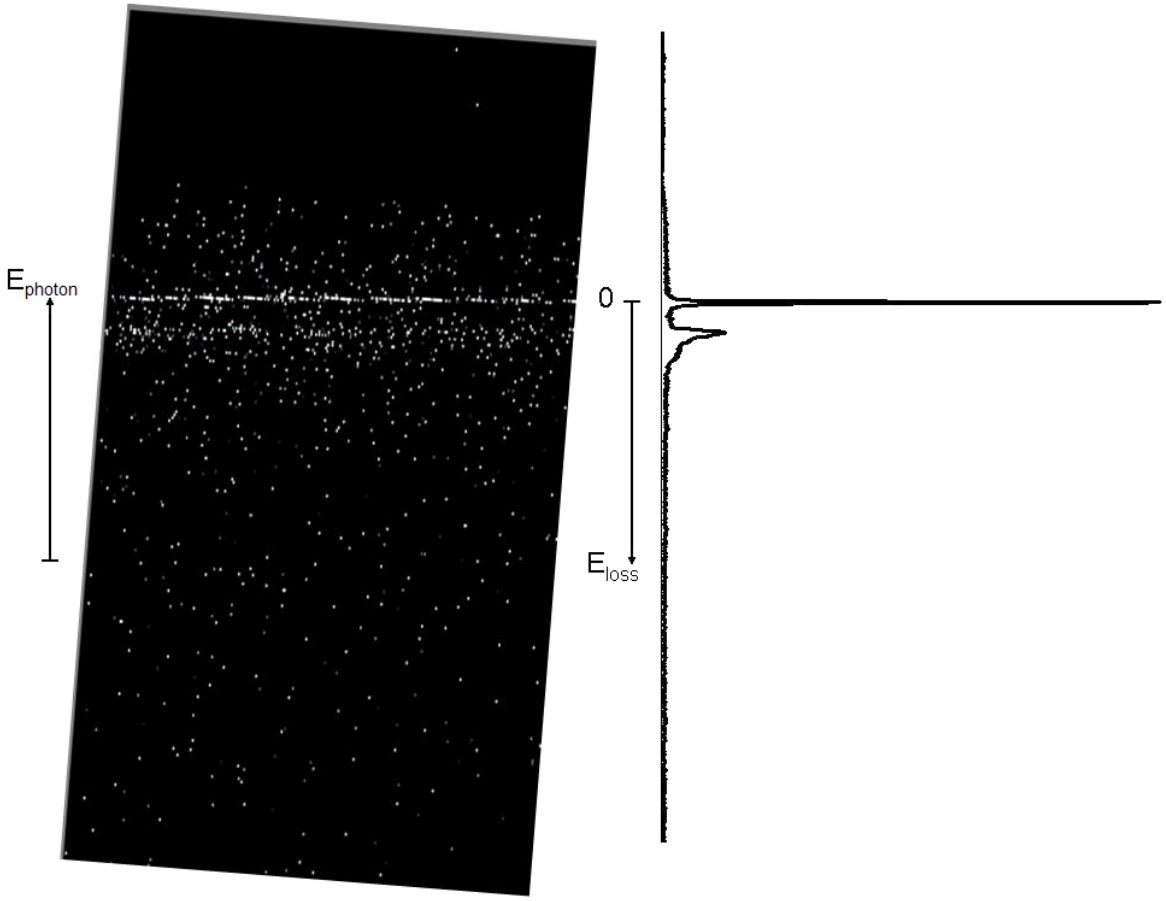

Figure 2.15: Raw image on the CCD and relative spectrum extracted (see the text for details).

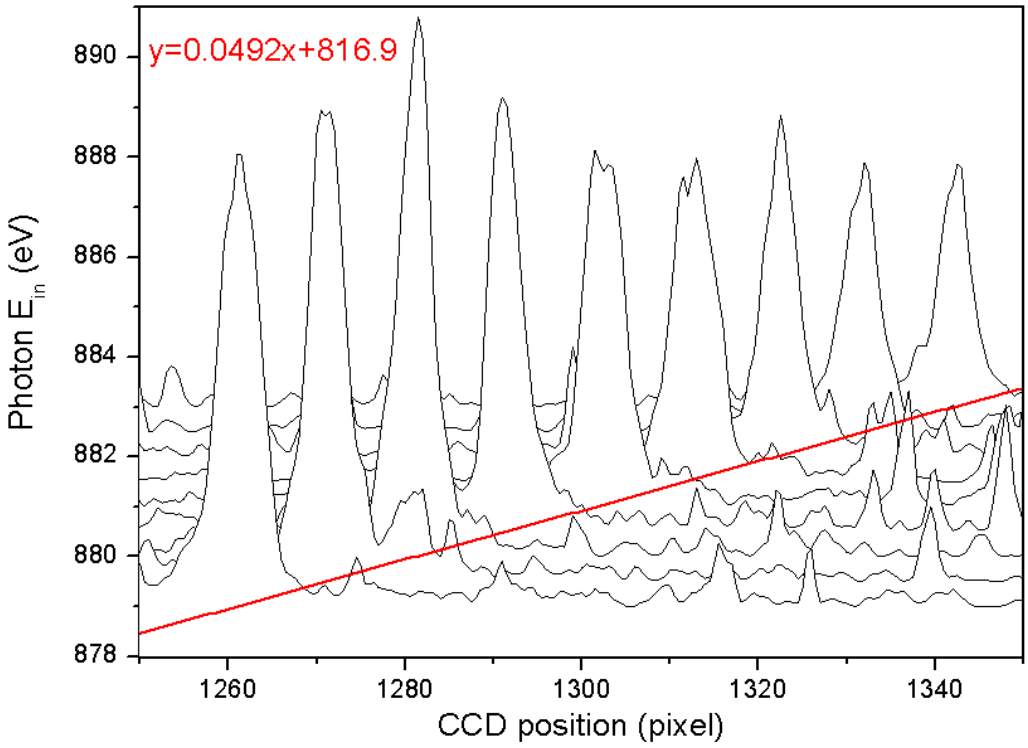

Figure 2.16: Calibration curve eV/pixel: incident photon energy versus peak position. In this case the calibration was 49.2 meV/pixel.

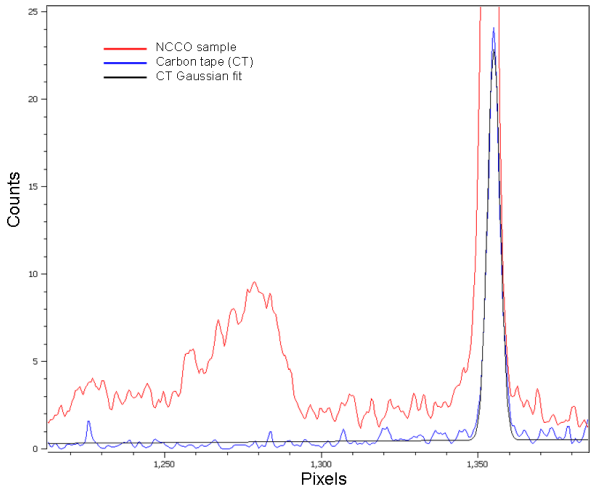

Figure 2.17: Example of NCCO spectrum aligned to its carbon tape reference. The Gaussian fit of this elastic peak has FWHM of 4.88 pixels, corresponding to 240 meV.

Chapter 3

Samples

In the present chapter a description of the three Cerium compounds analyzed by XAS and RIXS will be presented, followed by the electronic structure of Ce atom.

3.1 Three Cerium compounds

In *Figure 3.1* are shown the three samples we measured, $Nd_{1.84}Ce_{0.16}CuO_4$, $CeCu_2Si_2$ and $CeRu_2P_2$, glued onto the RIXS sample holder. Its peculiarities like the carbon tapes, the YAG screen and the razor blade have been explained in *Section2.2*.

- **$Nd_{1.84}Ce_{0.16}CuO_4$** (NCCO) is a high-T_c cuprate superconductor. Cuprates are 2D layered materials with CuO_2 planes in which electrons couple with spin excitations, instead of phonons, in forming superconductive Cooper pairs. In NCCO the Cerium atom is strongly hybridized with CuO_2 planes, acting as electron doper, thus activating superconductive behaviour [28]. In particular, 4 electrons are involved, so that Cerium is considered as a Ce^{4+} ion. The electronic configuration is thus $|4f^0\rangle$. Nevertheless, it has been shown [29] that in this compound the Ce atom can gain an electron from the hybridization with the Cu $3d$ valence band, so that an other possible configuration is $|4f^1\underline{v}\rangle$ (where $\underline{v}$ stands for a hole in valence band). The description of the real ground state configuration is therefore a (gerade) linear combination of the two.

- **$CeCu_2Si_2$** was the first evidence that superconductivity can exist also in a $4f$ material [30], where localized magnetic moments should be incompatible with the conventional BCS theory for superconductors. This compounds belongs to the class of *heavy fermion materials*, unfilled f-shell intermetallics where conduction electron gas properties are very influenced by many body interaction; at very low temperatures they show a pronounced peak of specific heat (and therefore a huge effective mass of the f electrons). In this case superconductivity arises thanks to these quasiparticles. The Cerium atoms in the compound are a mixture of Ce^{3+} and Ce^{4+} ions, with ratio $10:1$ [31].

- **$CeRu_2P_2$** can be used as comparison with $CeCu_2Si_2$ because they are almost isoelectronic, being in this case 3 valence electrons involved in chemical bonds, and isostructural: they both belong to the class of $ThCr_2Si_2$-type compounds.

We selected NCCO and $CeCu_2Si_2$ in particular because there is a good availability of high quality single crystals, in fact several groups have improved growth techniques for these

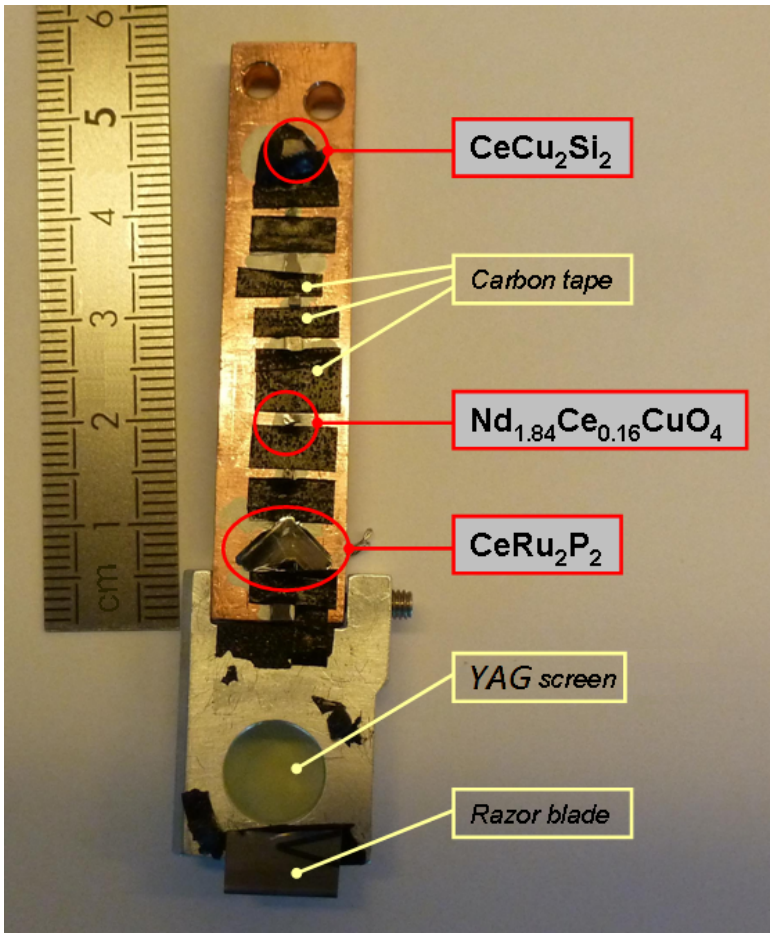

Figure 3.1: Sample holder for the spectrometer at beamline ID08, ESRF, with $CeCu_2Si_2$, $Nd_{1.84}Ce_{0.16}CuO_4$ and $CeRu_2P_2$ among other samples. Carbon tape references for each sample, the YAG screen and the razor blade are also shown (for details see *Sections 2.2.2* and *2.2.3*).

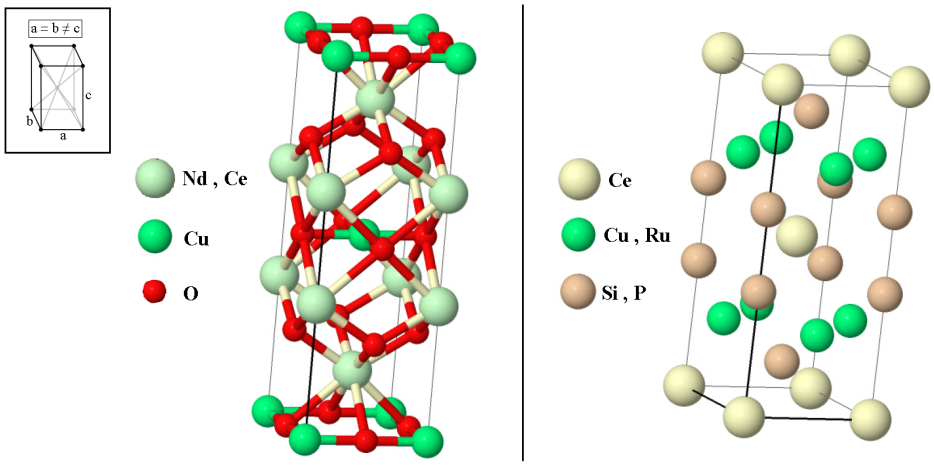

Figure 3.2: Crystal unit cell of $Nd_{1.84}Ce_{0.16}CuO_4$ (left) and of $CeCu_2Si_2$ and $CeRu_2P_2$ (right). In the inset is shown the body-centered tetragonal crystal system.

samples due to the high interest in their Physics. Our samples were made in Max Planck Institut für Chemische Physik fester Stoffe, Dresden, by S. Seiro, N. Caroca-Canales and C. Geibel. Because the samples have different valence, they can be useful in a comparison of RIXS spectra from different $4f$ configuration. In fact, the presence or not of a $4f$ electron during the scattering process should significantly influence the channels of energy losses. These results will be discussed in *Chapter 4*. In addition, we chose also $CeRu_2P_2$ because, compared to $CeCu_2Si_2$, it has a fourth raw transition metal (Ru) instead of third one (Cu), so that its ionic radius is bigger. This should increase the strength of the Crystal Field, even if its symmetry is the same, so that quantitative differences in RIXS should be expected.

3.1.1 Crystal unit cell

In *Figure 3.2* the structure of the unit crystal cell for NCCO and for $CeCu_2Si_2$ and $CeRu_2P_2$ are shown on left and right, respectively.

In NCCO 2D planes with Cu and O atoms are visible, alternated to a complex structure of Nd and O, where some Ce atoms substitute the Nd ones acting as electron doper for the CuO_2 planes. The whole structure is known as *perovskite structure*, and it is common to all superconductor cuprates. The other two samples have the *$ThCr_2Si_2$ structure*: a transition metal prism and a non metal double capped prism inscribed into a $4f$ element body-centered prism. Note how in both cases the prism base is a square.

Even if different, these two structures share the same *tetragonal crystal system*, i.e. they are rectangular prism with a square base $a \times b$ and height c, with $a = b \neq c$ (see the inset in *Figure 3.2*). In particular they belong to the $I_{4/m\,2/m\,2/m}$ Space Group in full Hermann-Mauguin notation, where I stands for body-centered lattice type and $4/m\ 2/m\ 2/m$ is the ditetragonal-dipyramidal Point Group (D_{4h} in Schönflies notation). This means there are one 90° rotational axis (parallel to c) with a perpendicular mirror plane and two 180° rotational axis (parallel to a and b) with their perpendicular mirror planes.

A given Cerium atom in these structures is thus expected to be experienced of a Crystal Field generated by the surroundings having the same space symmetry, i.e. with two equivalent directions a and b and a distinguished third one c.

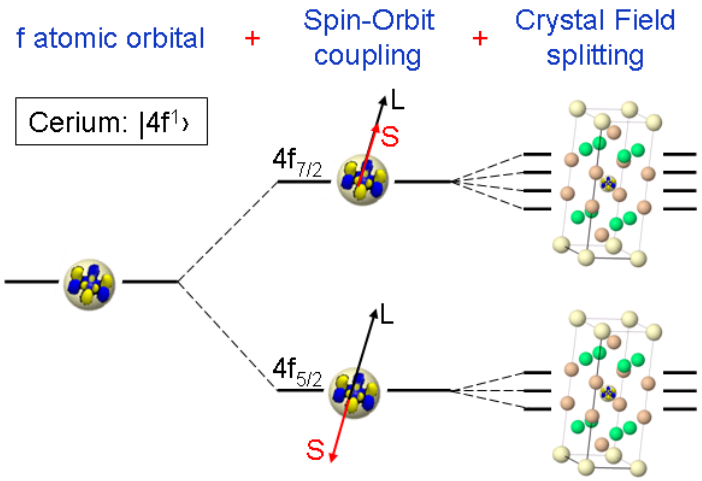

Figure 3.3: Scheme of Cerium $4f$ shell electronic structure. Spin-Orbit splitting is first shown, and then Crystal-Field effects, in this case with tetragonal symmetry.

3.2 Cerium electronic structure

According to the *Aufbau principle* the Cerium atom ground state electron configuration is:

$$[Ce] = [Xe]4f^1 5d^1 6s^2.$$

Let us consider the $4f$ shell. It contains only one electron, so that, according to Hund's rules, the value of its quantum orbital momentum is $L = 3$ and of its spin is $S = 1/2$. If they don't interact, two degenerate levels are possible, corresponding to the spin parallel or antiparallel to the orbital momentum. Nonetheless, because of *Spin-Orbit* interaction, as well-known, a good quantum number for the description of the system is the total angular momentum J, and the two levels are splitted: being $4f$ shell less than half-filled $J = L - S = 5/2$ correspond to the lower state (term symbol $^2F_{5/2}$), having the spin antiparallel to the orbital momentum, and $J = L + S = 7/2$ to the upper state (term symbol $^2F_{7/2}$), with the spin parallel (for details, see [11], for example). This is shown in *Figure 3.3*. The separation in energy is the difference between the two configuration energies, calculated as $\Delta \sim 300$ meV in this case. It is noteworthy that Cerium can be a Ce^{3+} ion, with $4f^1$ configuration, or Ce^{4+} ion, with $4f^0$ configuration. In the first case there is a $4f_{5/2}$ electron, while in the second the whole f shell is empty.

When we leave the atomic picture and we consider the atom in a certain compound, the $4f$ electron could be affected by the environment even if it is well localized (see *Figure 1.1*), and it could have dispersive behaviour. This would have important consequences on the material properties because such electron is very close to the Fermi level.

The average charge distribution in the surroundings coming from ions and electrons can be modelized as an electric field, namely a *Crystal Field* (CF), so that the $4f$ electron is not unperturbed anymore. The effect of the CF is the splitting of the $(2j+1)$-fold degeneracy of each SO level, depending on the particular symmetry of the system. A limit to the splitting is given by the *Kramers theorem*: a time-invariant system containing an odd number of fermions has a two-fold degeneracy at least.

In the case of Ce^{3+} under a generic CF there are 6 and 8 states for the ground and the first excited level, respectively. Starting from the highly symmetric situation without CF and $6-$ and $8-$ fold degeneracy, when the symmetry is reduced degeneracies are removed, up to the limit of three and four Kramers doublets. For instance, in cubic symmetry ${}^2F_{5/2}$ is splitted into doublet-quartet configuration, and ${}^2F_{7/2}$ into doublet-quartet-doublet. In tetragonal symmetry, on the other hand, all degeneracy are lifted, so that ${}^2F_{5/2}$ is splitted into three doublets configuration, and ${}^2F_{7/2}$ into four doublets [32]. This is the case of our samples, as described before, and it is shown in *Figure 3.3*. It is noteworthy that depending on the CF parameters the actual value of the split is different, as well as the positioning of the levels respect to E_F.

Chapter 4

Results and discussion

In the present chapter our results on Ce intermetallic compounds described in *Chapter 3* are shown. First the measure of the valence is reported, and then the presence of the Crystal Field is discussed. The third section is the main topic: the measure of low energy excitations by means of RIXS. Finally, higher energy features in RIXS spectra are also shown.

4.1 Determination of Cerium $4f$ configuration by means of XAS

As discussed in *Section 2.1.1* X-ray Absorption Spectroscopy can bring several information about the valence state and electronic structure of a certain element in a material thanks to its elemental selectivity. We measured the absorption at M_5 and M_4 edges of Ce atom, that are at ~ 883 eV and ~ 902 eV respectively [33], in three different compounds: $Nd_{1.84}Ce_{0.16}CuO_4$ (NCCO), $CeCu_2Si_2$ and $CeRu_2P_2$. In *Figure 4.1* the XAS measured in Total Electron Yield (TEY) mode at $M_{4,5}$ of the three samples is shown. The features of NCCO spectrum are clearly different from $CeRu_2P_2$'s one, whereas $CeCu_2Si_2$ spectrum has features in common with both the others. It is noteworthy that, as discussed in *Chapter 3*, $CeCu_2Si_2$ exhibits mixed valence behaviour.

In order to better recognize the differences in the valence numbers we performed XAS measurements also on six different reference samples, as reported in *Figure 4.2(a)*. Because of the strong electronegativity of the fluorine, the formal oxidation state of ionic cerium in CeF_3 is 3+, so that the ground state can be well assumed [21] as $|4f^1\rangle$. This is a reference sample that was measured in our setup at beamline ID08 (ESRF) during each XAS acquisition, as reported in *Section 2.2.2*.

As well established in literature [21], on the other hand, a good reference sample for a chemically tetravalent cerium is CeO_2 (considering -2 as oxidation number of O), whose ground state is physically described by the combination of states $|4f^0\rangle$, $|4f^1\underline{v}\rangle$ and $|4f^2\underline{v}^2\rangle$ because of the hybridization between Ce $4f$ and O $2p$ states. In a first analysis the $|4f^2\underline{v}^2\rangle$ state will be disregarded, being its relative weight typically neglectable.

The other four reference samples are shown in *Figure 4.2(a)* from top to bottom with increasing relative weight of valence 3+, corresponding to decreasing relative weight of 4+. Note the arising peak at 881.5 eV, and the two disappearing features at 887.5 eV and 883 eV, that are fingerprints of trivalent and tetravalent references, respectively. Also at the M_4 edge trivalent and tetravalent peaks are identified, the former at 896 eV and 897.5 eV, the latter

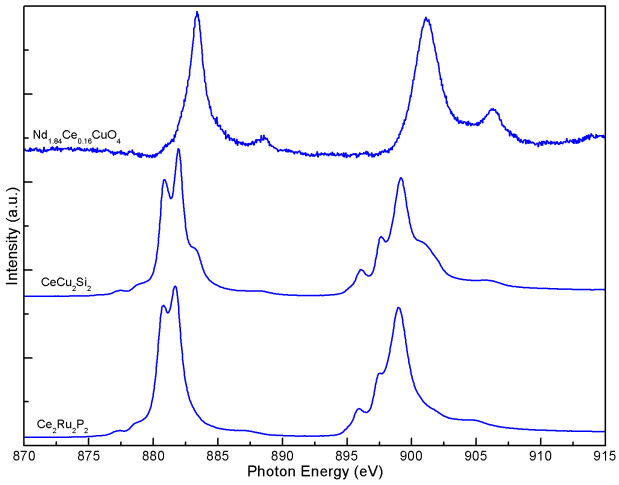

Figure 4.1: XAS (TEY) $M_{4,5}$ edges of NCCO, $CeCu_2Si_2$ and $CeRu_2P_2$ (measurement performed at ID08, ESRF).

at 906 eV and 900.5 eV.

In *Figure 4.2(b)* the three samples, reported in the center, are now compared with the tetravalent and trivalent references, on top and on bottom, respectively. What can be observed in this order for the samples is a sort of transition from 4+ to 3+ valence state of Cerium atom. Indeed, NCCO spectrum is well comparable to the 4+ reference, whereas $CeRu_2P_2$ spectrum seems very similar to the 3+ reference. $CeCu_2Si_2$, in the middle, shows a trend that is mainly trivalent, but two shoulders (marked with arrows in the figure) at higher energies in both edges are in correspondence of the main feature of the tetravalent reference. Differently from the reference sequence of *Figure 4.2(a)*, however, this shoulders are well visible even when the main peak at 881.5 eV of the trivalent atom is emerged, whereas in the references they are almost suppressed, as in $Ce_2(SO_4)_3$. This suggests that the spectra have different weights for the mixed valence states.

4.1.1 Total Electron Yield versus Fluorescence Yield

Whereas TEY can be directly related to the absorption cross-section, FY is a radiative process that has to obey to dipole selection rules, as discussed in *Section 2.1.1*. In *Figure 4.3* TEY measurements of the samples are compared with FY. The general trend in FY is a suppression of the strong channels whereas weaker are enhanced. This can be related to the *self-absorption* and *saturation* effects [34]. Nevertheless, some peaks do not follow this trend, such as the features at 879 eV and 896 eV. They could be due to the multiplet structure of the excited state from which fluorescence emission occurs [35], which can alter the spectrum. It can be evaluated when considering the *total emission spectrum* (TES), obtained from RIXS measurements [36]. This two topics will be now shortly discussed.

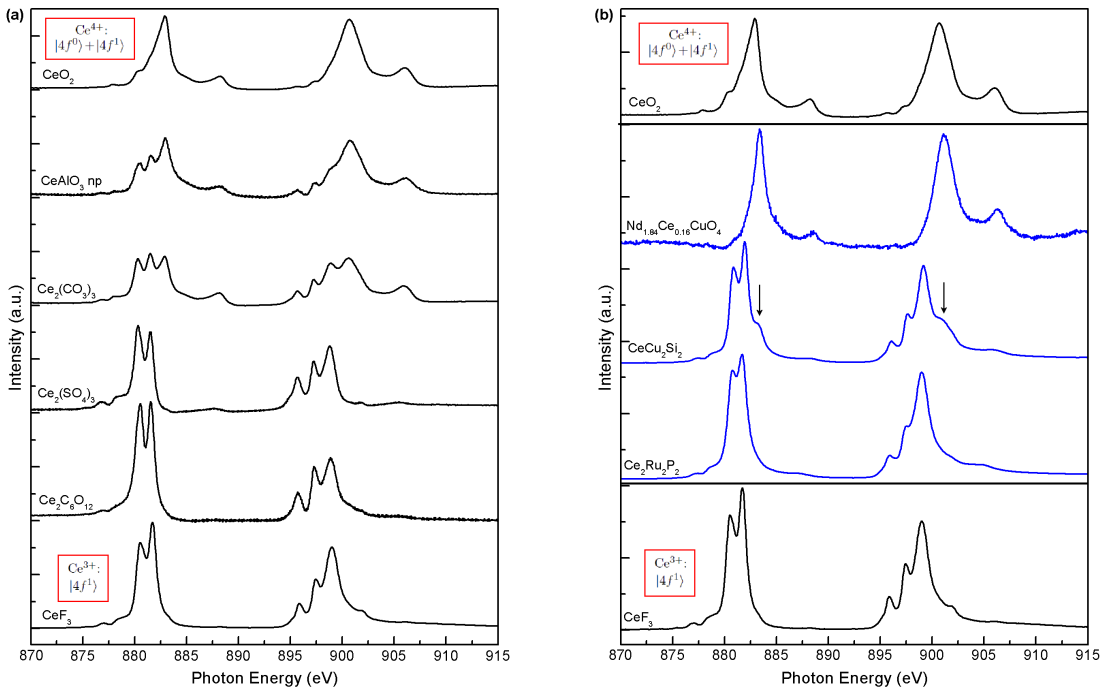

Figure 4.2: XAS (TEY) $M_{4,5}$ edges of references and samples. *Panel (a)*: references CeO_2, $CeAlO_3$, $Ce_2(CO_3)_3$, $Ce_2(SO_4)_3$, $Ce_2C_6O_{12}$ and CeF_3. A valence number transition from 4+ to 3+ can be observed. *Panel (b)*: Up and down, respectively, tetravalent CeO_2 and trivalent CeF_3 references. In center, NCCO, $CeCu_2Si_2$ and $CeRu_2P_2$ samples. Arrows mark mixed valence feature of $CeCu_2Si_2$. Measurement performed at ID08, ESRF.

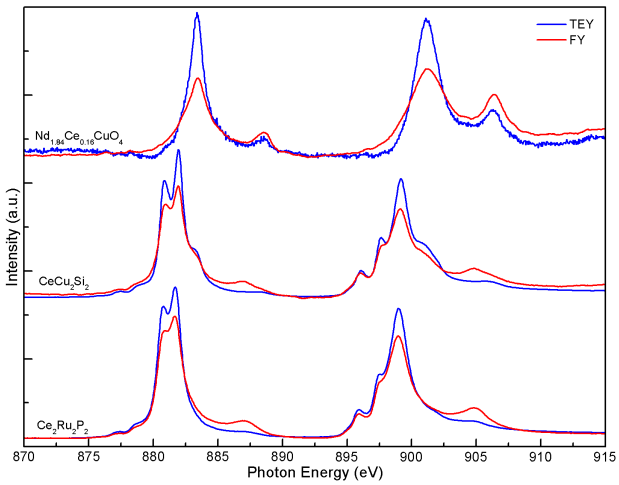

Figure 4.3: Comparison between TEY (blue) and FY (red) of NCCO, $CeCu_2Si_2$ and $CeRu_2P_2$ (measurement performed at ID08, ESRF).

Self-Absorption and saturation

Since TEY is largely dominated by surface effects because of the limited escape depth of the electrons, FY has been introduced in order to probe bulk properties. Nevertheless, in soft X-ray range if the sample is not thin enough it will absorb *also* fluorescence photons generated by the resonant incident ones, in addition to these themselves. This is called *self-absorption*, and it will reduce and broaden the relative intensity of the more intense absorption channels, in favour of the weaker ones. Absorption cross-section is thus not directly proportional to the fluorescence yield, and this has strong dependence on the experimental geometry: the more the detector is tilted respect to the sample surface, the more the spectra suffer from self-absorption distortion.

In addition, the intensity of the incoming photons is not constant when passing through a thick sample, because they are strongly absorbed at certain resonance energies. Thus at deeper layer of the sample those energies are less absorbed, because the intensity is lower. This is known as *saturation* effect, and its result on the spectra is the same of Self-Absorption: the relative intensity of stronger and weaker absorption peak is reduced, and this is present in our measurement of *Figure 4.3*.

Total Emission Spectrum

When the lifetime of the excited state reached by absorption and from where fluorescence starts is short, fluorescence spectra are affected by resonance effects due to the coupling of emission and absorption, so that it is necessary to consider them together as a second order scattering [37]. In support of this idea the Total Emission Spectrum (TES) has been introduced [36]: it is the measure at an angle of the emitted photon intensity integrated over outgoing photon energy as a function of incident photon energy; basically it is a RIXS spectrum *without* energy resolution.

It is expected that TES, a second order measure, will show features that are present in FY absorption spectra and not in TEY. Indeed, FY can be affected by the multiplet structure of the intermediate state of scattering process, from which inelastic scattering can occur. This has been proved, for example, in a thin film of Thulium [35]. In *Figure 4.4(a)* the M_5 absorption edge of Tm is shown, measured with transmission (solid line), TEY (crosses) and FY (dots). Whereas TEY fits all features of the transmission measurement, that is the most directly connected to the absorption cross-section, FY has the peak labeled as A clearly suppressed.

Figure 4.4(b) shows the scattered photon intensity as a function of the outgoing photon energy, i.e. a plot related to the RIXS spectrum, for three different incoming photon energies corresponding to the three peaks of *Figure 4.4(a)*, with the zero energy chosen at the peak B position. All the spectra A,B and C, dots, crosses and solid line respectively, show a peak at energy equal to that of the incoming photon. Being the integral of this elastic contribution much higher for spectrum B than A and C, the FY spectrum of *Figure 4.4(a)* can be described as a main peak at B position and two smaller shoulders at A (marked by an arrow) and C positions. However, RIXS spectrum C has in addition an inelastic contribution at 4.5 eV from its elastic peak, due to transition toward a multiplet final state, which considerably contributes to the integral. For this reason the peak C in FY is enhanced, whereas A is not, being due only to the elastic scattering.

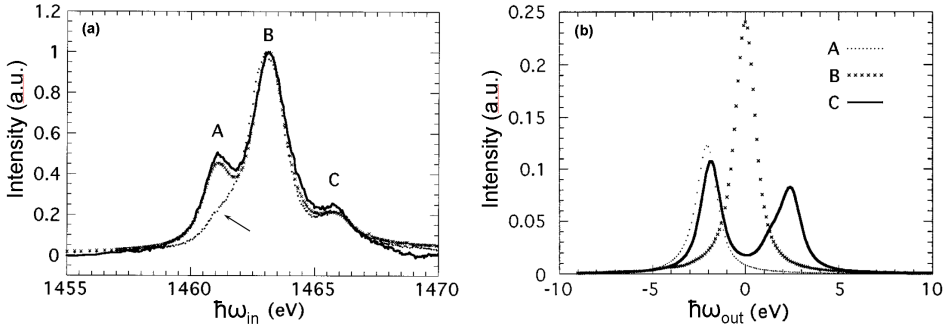

Figure 4.4: X-ray absorption and scattering from Tm thin film. *Panel (a)*: absorption with transmission mode (solid line), TEY (crosses), and FY (dots). Three channels A,B,C are identified. *Panel (b)*: resonant scattering for three different energies labeled in *panel (a)*, peak A (dots), peak B (crosses) and peak C (solid line). The zero of the outgoing photon energy is chosen at peak B position. Pictures from [35].

Returning to our data, it is possible to interpret FY of *Figure 4.3* considering the TES. In a simple energy level diagram like that of *Figure 2.9*, in *Figure 4.5* are shown two RIXS spectra (as histograms, without broadening, for simplicity) obtained with resonant incident photon energy A (blue) and B (red). Each spectrum, when integrated over the outcoming photon energy, gives a peak in the Total Emission Spectrum.

Let us consider for example $CeCu_2Si_2$. In this case, we measured RIXS spectra for eleven different energies around the M_5 resonance. The integral of each of these spectra gives a delta function in the TES, as shown by square dots in *Figure 4.6*. It can be compared to the FY (red line), where there is some agreement. This can mean that FY is not directly related to the absorption, not only because of Self-Absorption and Saturation effects, but also inelastic contributions have to be considered. However it is important to notice that TES spectrum is strongly dependent on the number and the energy position of delta functions considered, so that TES alone cannot fully reproduce the shape of the FY if the number of points is not sufficient, as for the discrepancy in the main peak at 881.5 eV in our case.

4.2 Presence of Crystal Field in XAS measurements

In *Figure 4.7* a calculation of XAS spectra with increasing Crystal Field D_q parameter in cubic symmetry (for simplicity) is shown for the Ce^{3+} atom. Lifetime broadening has been considered, different for the two edges: Lorentzian lineshape with FWHM of 800 meV for the M_5 and 1300 meV for the M_4. A Gaussian convolution has been done in order to consider the experimental resolution, evaluated as 200 meV of FWHM. They are all qualitatively consistent with our $CeCu_2Si_2$ and $CeRu_2P_2$ data. The main trend from the isolated atom ($D_q = 0$ meV) to the CF affected one with $D_q = 300$ meV is a reduction of the peak at 882 eV, while that at 880.5 eV increases. The ratio between this two peaks in the two cases is 2.03 and 1.36 respectively. In our data this ratio is ~ 1.08, suggesting a presence of CF (cubic) distortion.

As discussed in *Section 2.1.1*, X-ray Linear Dichroism can be interpreted as sign of non isotropic absorber center, i.e. in case of spherical symmetry breaking. At beamline ID08,

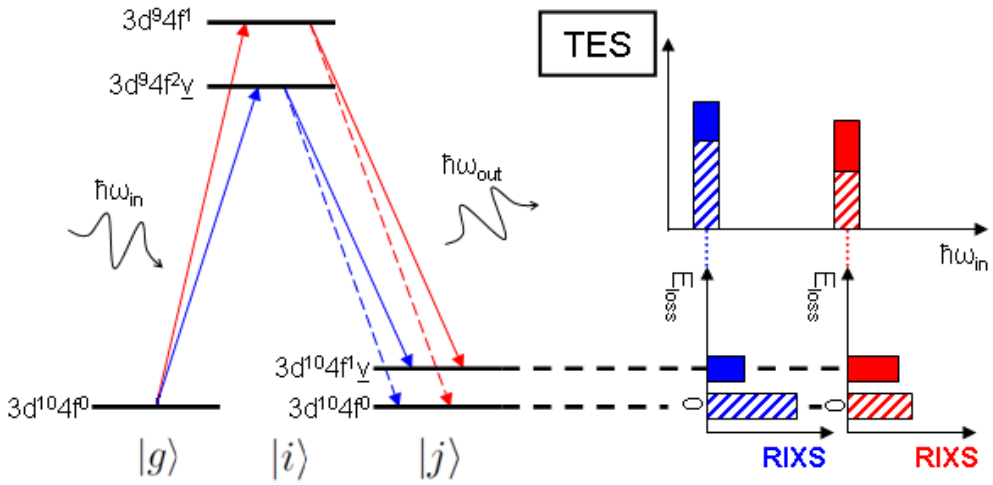

Figure 4.5: Example of a Total Emission Spectrum (TES) obtained from RIXS spectra with two different energies (blue and red). The integration of each RIXS spectrum over E_{loss} gives a peak in TES. For simplicity peaks are represented by rectangles. Each RIXS spectrum has elastic (dashed line) and inelastic (solid line) contribution, coming from the multiplet final state $|j\rangle$, as shown in the energy level diagram of resonant $3d \rightarrow 4f \rightarrow 3d$ transitions for Ce (figure adapted from [36]).

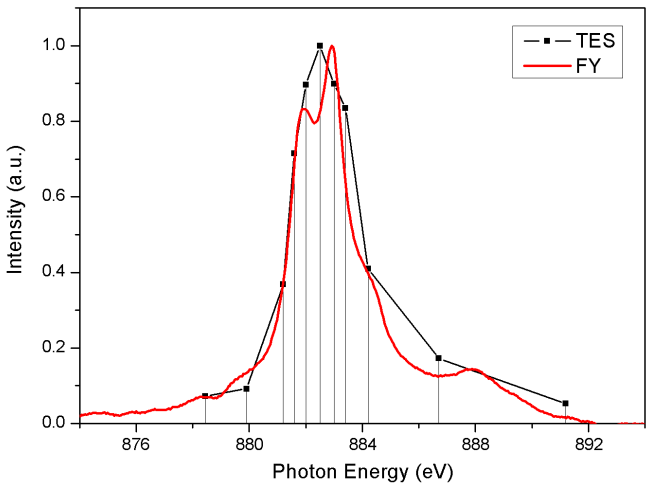

Figure 4.6: TES for $CeCu_2Si_2$, obtained with eleven different RIXS spectra around M_5 edge (connected dots). The FY is shown in red line (measurement performed at ID08, ESRF).

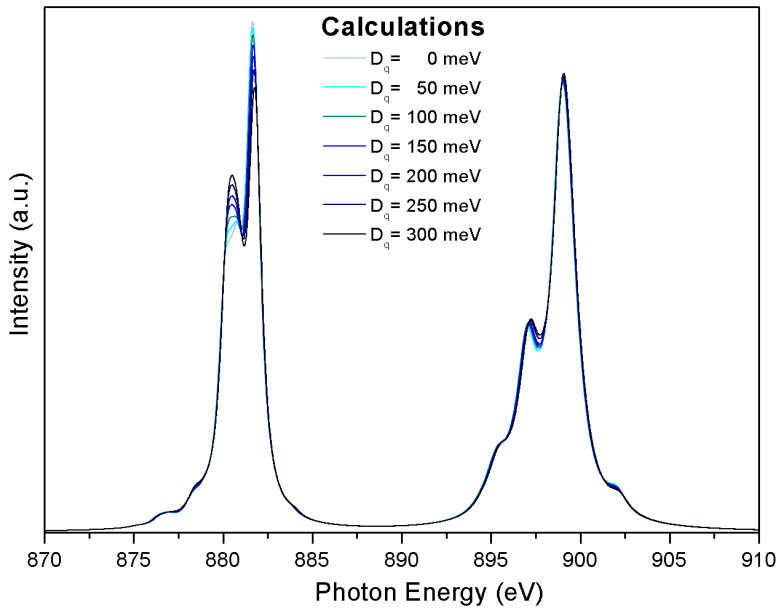

Figure 4.7: Calculation of cubic CF effects on Ce^{3+} absorption spectrum. Variations with increasing D_q parameter from 0 meV (no CF) to 300 meV are shown. 'Missing' code [38] has been used for the atomic multiplet calculation, and 200 meV of FWHM for the Gaussian experimental resolution have been considered, convolved with a Lorentzian broadened spectrum (800 meV and 1300 meV FWHM for the $M_{4,5}$ edges).

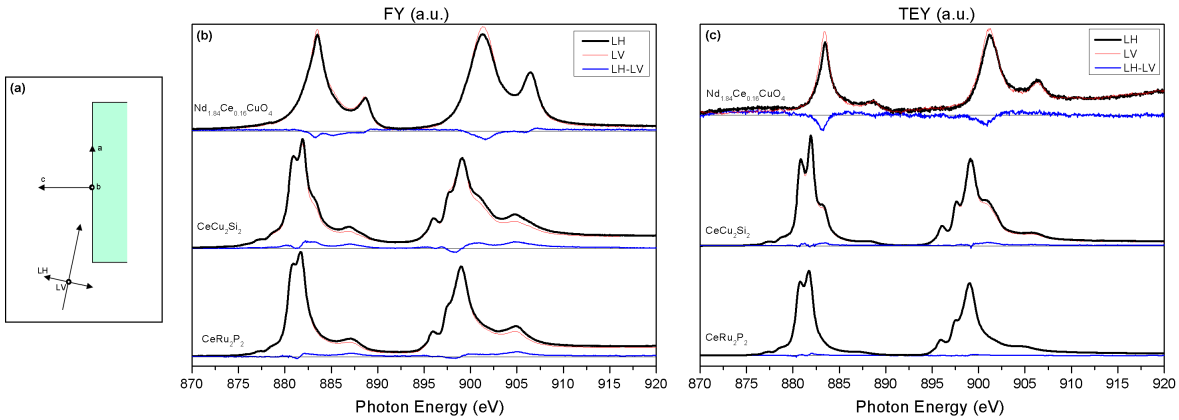

Figure 4.8: X-ray Linear Dichroism. *Panel (a)*: grazing incidence setup, where LV polarization has **E** field in the **b** direction, while LH in the **c** direction and a small component in **a**. *Panel (b)* and *(c)*: FY and TEY with LH (black) and LV (red) polarization, and dichroism signal $LH - LV$ (blue), at $M_{4,5}$ edges of NCCO, $CeCu_2Si_2$ and $CeRu_2P_2$. Measurement performed at ID08, ESRF.

ESRF, is possible to set the undulators in order to obtain $\sim 100\%$ linearly polarized incoming X-rays, for instance with LH and LV (horizontal and vertical respect to the synchrotron plane) polarization.

In our experiment the samples were oriented with the two equivalent **a** and **b** axis in the surface plane, and the **c** axis perpendicular to it (see *Chapter 3*). As shown in *Figure 4.8(a)*, in a grazing incidence setup it is possible to probe the anisotropy of the electronic states by choosing LV polarization, with the incoming **E** field parallel to **b**, and LH polarization, with **E** in the **c** direction and a small component in **a**.

We performed X-ray Absorption Spectroscopy with both polarizations on the three samples in order to evaluate the dichroism signal as $LH - LV$. The presence of dichroism is a sign of distortion of the unit crystal cell, and thus of presence of anisotropic non-cubic Crystal Field in our Ce compounds. In *Figure 4.8* are shown the FY (*panel (b)*) and the TEY (*panel (c)*) for the three samples with LH (black) and LV (red) polarization, and the XLD signal (blue). NCCO data are normalized to the spectra integrals, while $CeCu_2Si_2$ and $CeRu_2P_2$ are normalized to their M4 highest white line; in addition, FY data have been before scaled to their pre-edge.

In all the cases the dichroism is small, so that tetragonal CF distortion of the cubic symmetry is difficult to be detected, and it is only suggested. However this is in agreement with the localization of the $4f$ orbitals, for which effects due to the surroundings should be small.

4.3 Sub-eV excitations of the $4f$ shell probed by RIXS

As discussed in *Section 2.1.2* Resonant Inelastic X-ray Scattering gives us further information respect to XAS being a second order process. We performed RIXS on the M_5 edge of Ce atom in the three samples $Nd_{1.84}Ce_{0.16}CuO_4$ (NCCO), $CeCu_2Si_2$ and $CeRu_2P_2$. Qualitative differences are expected for the Ce ion 4+ and 3+, as it will be first described, and then

measurements will be shown and discussed.

4.3.1 Dependence of X-ray scattering on the $4f$ shell occupation

Depending on the $4f$ shell configuration, soft X-ray scattering from Cerium atom will show different features. In order to better understand how the electronic structure is expected to be and to compare our measurements, we performed atomic multiplet calculations.

In the case of Ce^{4+}, corresponding to $4f^0$ configuration, only the elastic scattering is expected. In fact, when an electron from the $3d_{5/2}$ shell is excited into the empty $4f$ shell (M_5 transition) it is the only $4f$ electron which can decay from the intermediate state $|i\rangle$ to the finale state $|j\rangle$ during the RIXS process. This clearly means the scattering could be only elastic, without any kind of excitation between f levels. This is correctly reproduced by the calculated RIXS spectra shown in *Figure 4.9(a)*.

On the other hand, when considering a sample with Ce^{3+} ion, having a ground state $|g\rangle$ described by a $4f^1$ configuration, in addition to the elastic scattering an inelastic event becomes possible. In fact, when a $3d_{5/2}$ electron is promoted into a $4f$ level in the intermediate state $|i\rangle$, it could be possible that the *other* $4f$ electron makes the transition towards the $3d$ core hole by emitting an X-ray photon. The net result is a transition of an electron between two $4f$ levels. This is called ***ff* excitation**, meaning that a $4f$ electron - $4f$ hole couple is left into the system. This is shown in *Figure 4.9(b)*.

The calculation shown for Ce^{3+} is performed considering Spin-Orbit coupling. In order to better assign the inelastic feature in RIXS to a certain transition, in *Figure 4.10(a)* are reported the calculations in the case of full and 50% reduced Spin-Orbit strength parameter (center and bottom, respectively). What is clearly pointed out is that the splitting in two levels is a pure SO effect, because decreasing the SO coupling parameter the splitting is consequently reduced. According to *Section 3.2*, the two states are $^2F_{5/2}$ and $^2F_{7/2}$. In the case of full SO the energy splitting is evaluated as $\Delta \sim 300$ meV, in good agreement with ARPES measurements (see *Figure 1.3*). The *ff* excitation involving two levels with different total momentum is called ***jj* excitation**, or Spin-Orbit excitation (top of *Figure 4.10(a)*).

When introducing the Crystal Field in calculations further splittings are obtained. The symmetry considered is tetragonal, with CF parameters taken from [8]. As discussed in *Section 3.2*, with this symmetry $^2F_{5/2}$ state is finely structured into three sub-peaks and $^2F_{7/2}$ into four. This is correctly reproduced by the calculated RIXS spectra shown in *Figure 4.10(b)*. If the *ff* exciton in RIXS process belongs to two different CF levels with the same total momentum J, the excitation is known as **Crystal Field excitation** (top of *Figure 4.10(b)*).

In general, the presence of dichroism in RIXS can be due both to the absorption and to the emission process. In our case, however, dichroism signal in XAS is quite low (see *Section 4.2*), so the difference between LH and LV is ascribable to the scattering. From the comparison between LH and LV polarizations shown in *Figure 4.10(c)* (center and bottom, respectively) it is clear that the intensity of the inelastic features are comparable, while the elastic line is much higher in LV polarization than in LH. This polarization dependence can be interpreted by geometric considerations. The experimental RIXS setup had a scattering angle of 50° with the sample oriented at normal emission; in this configuration LH polarization is less sensible to the elastic scattering respect to LV. In fact, elastic scattering can be interpreted by a free electron oscillation model, so that the emission of a dipole in the vertical direction has a maximum in the normal direction, whereas only the in-plane component of the horizontal direction excited dipole emits light in the direction of the spectrometer (top of *Figure 4.10(c)*).

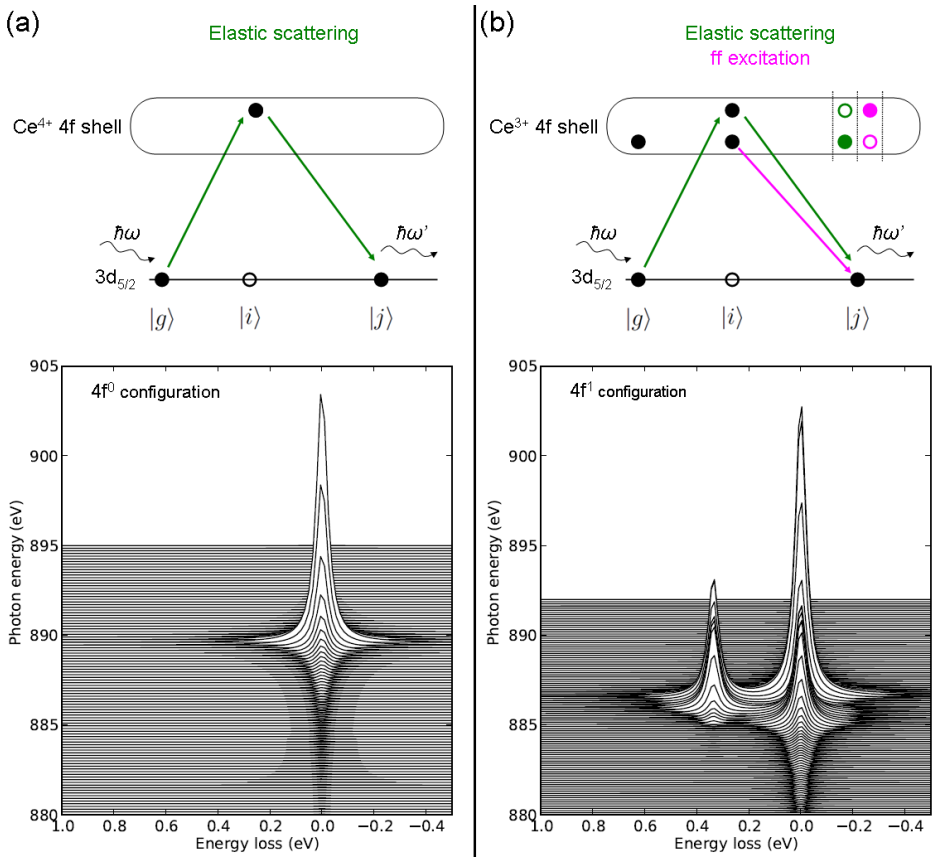

Figure 4.9: Scheme and Calculations of RIXS at M_5 edge for Ce^{4+} (panel (a)) and Ce^{3+} (panel (b)). In Ce^{4+} only the elastic scattering is possible, in Ce^{3+} *ff* excitations are also present. Atomic Multiplet Calculations performed with 'Missing' code [38].

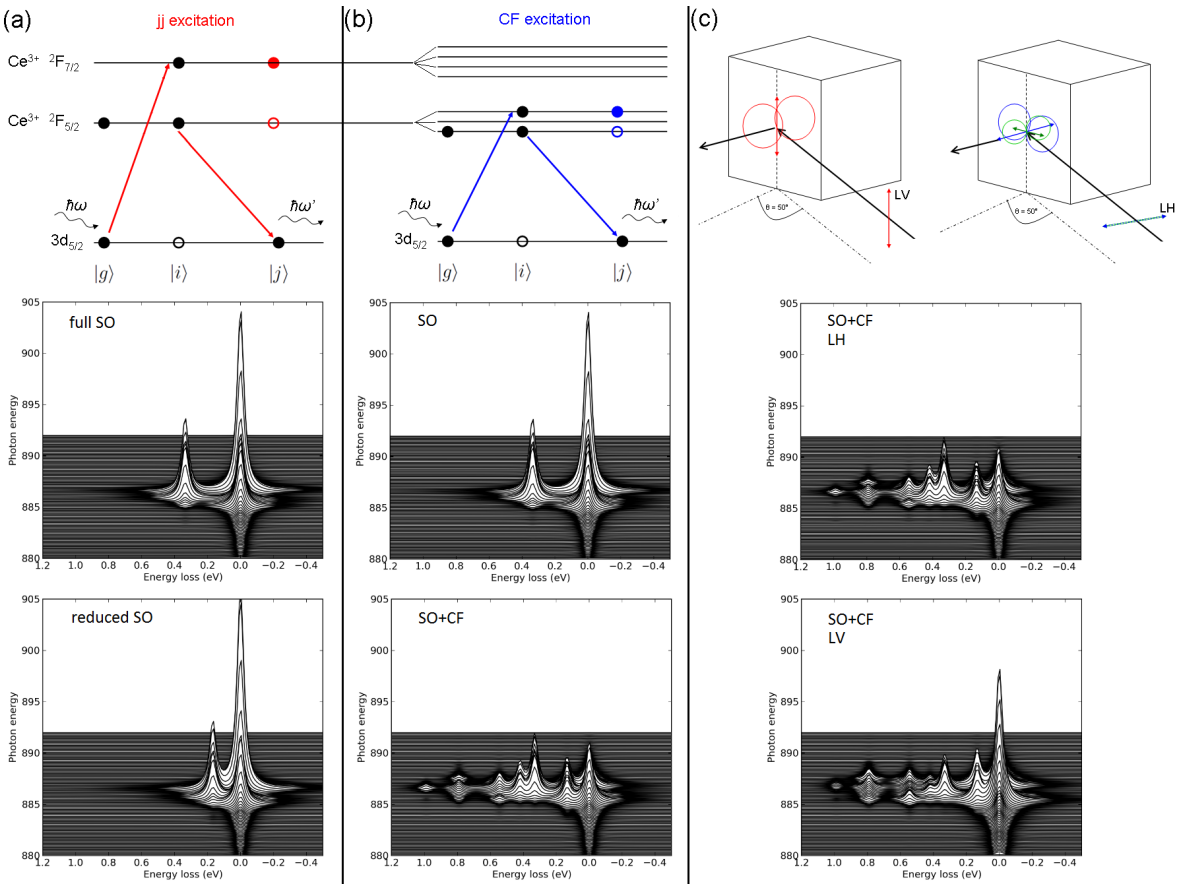

Figure 4.10: Panel (a): scheme of *jj* excitation (top) and calculations with full (center) and reduced (bottom) Spin-Orbit parameter. Panel (b): scheme of CF excitation (top) and calculations with only Spin-Orbit (center) and with Spin-Orbit and Crystal Field (bottom) splittings. Panel (c): scheme for the polarization dependence of the elastic line (top) and calculations with Spin-Orbit and Crystal Field splittings with LH (center) and LV (bottom) polarization. See the text for details. Calculations performed with 'Missing' code [38].

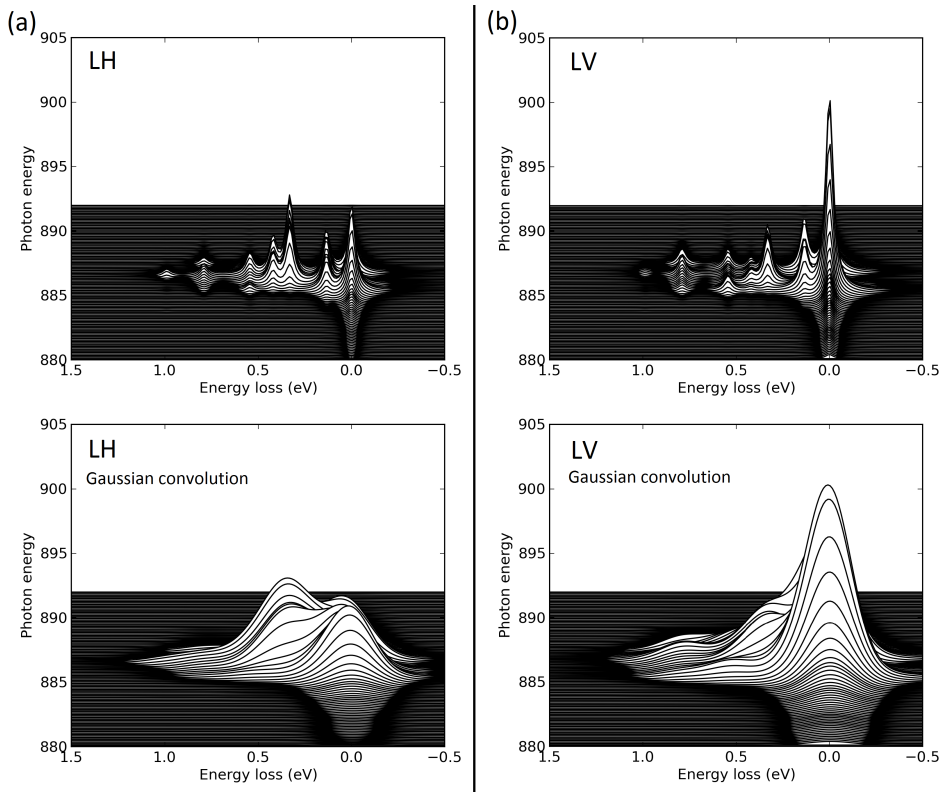

Figure 4.11: The spectrometer resolution of $\sim$ 250 meV is considered in calculations with a Gaussian convolution. LH and LV polarization are shown in panel (a) and (b), respectively. Only the *jj* excitation and the quasi-elastic features are now visible. Calculations performed with 'Missing' code [38].

The spectrometer resolution is estimated around 250 meV (see *Section 2.2.2*). Therefore in order to compare the measurements with the calculations, these have to be convolved with a Gaussian spectrum having FWHM of 250 meV. This is shown in *Figure 4.11* with LH (panel (a)) and LV (panel (b)) polarization. The CF levels result embedded in the elastic peak and in the *jj* excitation, the only inelastic feature clearly visible. Even if the CF structure is disappeared, the two features are broader than the resolution itself. This could be therefore a clue of CF structure. It is noteworthy that the inelastic feature, assigned to *jj* excitation, is comparable in the two polarization cases, while the quasi-elastic feature is more intense in LV than in LH because of the strong polarization dependence of the elastic line discussed before.

4.3.2 ff excitations in soft X-ray scattering

In *Figure 4.12* RIXS spectra with different incident photon energy around the M_5 edge on NCCO sample, having $4f^0$ configuration as discussed in *Section 4.1*, are shown. Spectra obtained with LH and LV incident polarization are shown in black and red, respectively. A 2D color map is also shown. For each of them only the elastic line is present, without any energy loss features near the zero. The variation in intensity can be related to the shape of the absorption spectrum. As discussed in *Section 4.3.1*, the LV polarization is more intense than the LH polarization.

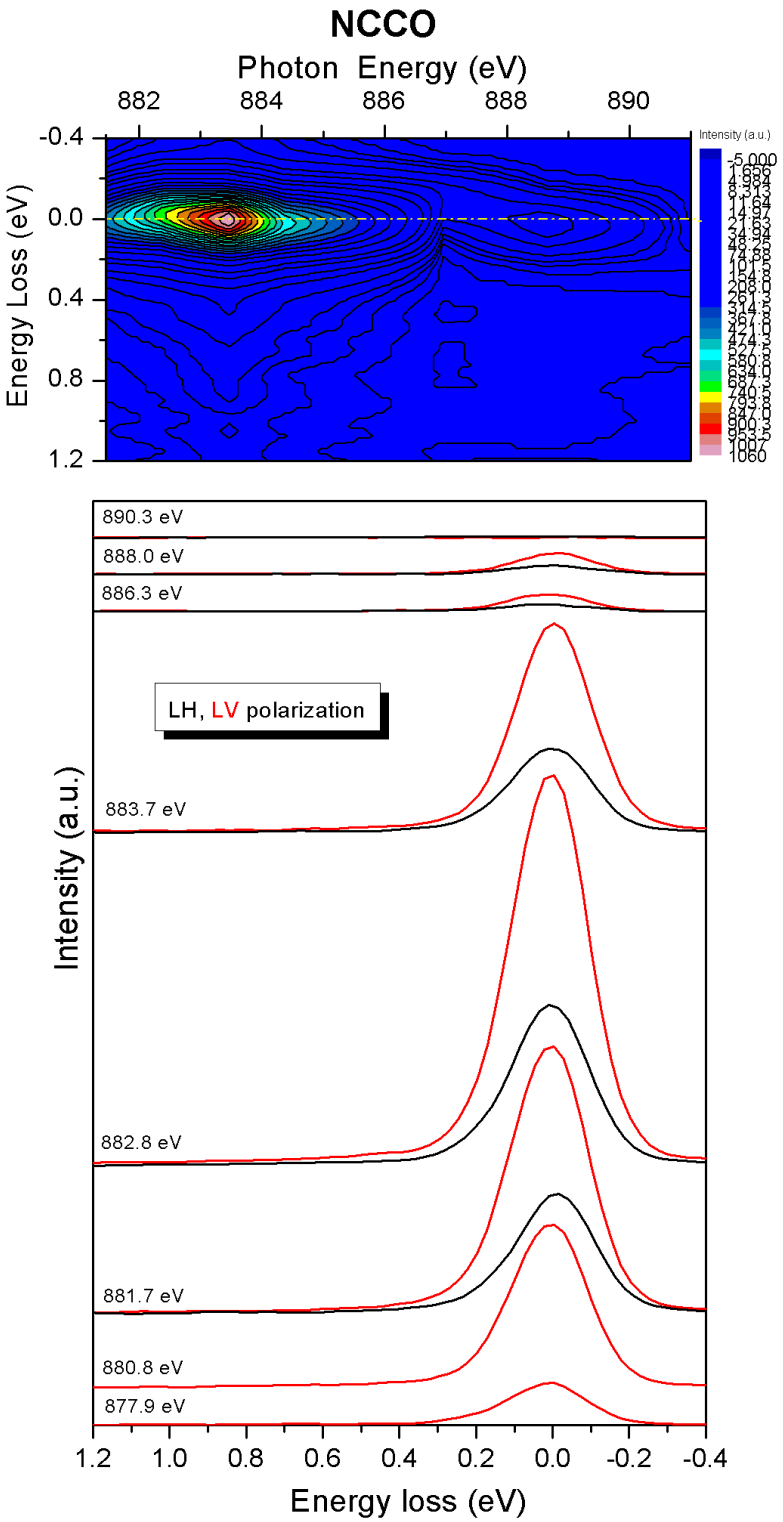

Figure 4.12: RIXS measurements on NCCO at M_5 Ce edge. Spectra with different incoming photon energy, aligned to their falling inflection point. Each spectrum comes from 40 min of acquisition. LH and LV polarization in black and red lines, respectively. A 2D color map is also shown for LH polarization. Measurement performed at ID08, ESRF.

In *Figure 4.13(a)* the whole set of RIXS measurements on M_5 Ce edge in $CeRu_2P_2$, having a Ce^{3+} ion as discussed in *Section 4.3.1*, is shown for both incident polarizations LH and LV (black and red, respectively). A 2D color map is also shown. In *Figure 4.13(b)* the same plot for $CeCu_2Si_2$ sample, having 3+ valence mixed with a 4+ contribution, is shown. In all the spectra are clearly visible two features. An inelastic one around 300 meV is identified as *jj* excitation. *This value is a direct measure of the Spin-Orbit splitting of the Cerium* $^2F_{5/2}$ *and* $^2F_{7/2}$ *states.* Note how the inelastic feature rapidly disappears when the incident photon energy goes out of resonance: in this case in fact it is possible only the elastic scattering, that contributes to the other feature [21]. This one contains both the elastic line and possible CF excitations. As mentioned before, with LH polarization the elastic line is suppressed respect to LV polarization: in this case the inelastic feature becomes more visible. Comparing $CeRu_2P_2$ with $CeCu_2Si_2$, the inelastic *jj* excitation is higher, respect to its own elastic line, in $CeRu_2P_2$ sample. This is in agreement with XAS results: while Ce in $CeRu_2P_2$ is more purely 3+, in $CeCu_2Si_2$ it is mixed with 4+, with the result that *ff* excitations become in general less favourite (being absent in Ce^{4+} as discussed before).

In both the inelastic and the (quasi-)elastic features there should be CF splitting but it is difficult to assert that they are actually finely structured, because of the clear lack of resolution. Nonetheless, when the energy is in resonance the *jj* feature seems somehow structured, even if this could be due to a small contribution from Ce^{2+} configuration, that could be present. An important result, that suggests further analysis with higher resolution spectrometers, is the fitting of RIXS data with Gaussian peaks, as shown in *Figure 4.14.* While the quasi-elastic feature is fitted by a Gaussian spectrum with FWHM comparable to the spectrometer resolution, the inelastic feature requires a broader peak, implying the presence of substructures. *Thus despite the limiting resolution hints of Crystal Field levels are observed by means of X-ray scattering.* The quasi-elastic feature is dominated by the elastic line, and this hides the CF excitations in the Gaussian fitting.

Angular dependence

All the measurements shown thus far have been performed with a normal emission experimental setup, i.e. $\delta = -25°$ being δ the anticlockwise angle from the bisectrix of the scattering angle toward the normal of sample surface. In general, depending on the incidence angle, CF excitons could show dispersion $E = E(\mathbf{k})$, where $\mathbf{k}$ is the transferred momentum.

In *Figure 4.15(b)* RIXS spectra at fixed 881.5 eV of incident photon energy are shown for different incident angles. These are chosen from $\delta = 0°$ to $\delta = 50°$ with steps of 10° (see *Figure 4.15(a)*). Being not able to resolve CF fine structure it is natural to do not have clear evidence of momentum dependence CF levels. Nonetheless, features seem to slightly move in opposite directions when the angle is varying, but this could merely be an effect of the varying intensity of the two features. In order to clarify this point, it is shown the fit of each spectrum with two Gaussian peaks, in addition to a third very broad Gaussian peak just to take into account the background. One of the two peaks (labelled as 1) was fixed at 0 eV of energy loss representing the elastic line (E_1), while the other peak position (E_2) and the two FWHM (G_1,G_2) were free parameters. The spectral shape is well reproduced at the various angles when the second peak is around 280 meV, without dispersing. What can be interestingly noted is that the FWHM of the first peak G_1 is around 230 meV, corresponding to the spectrometer resolution. This should have been the same FWHM for the inelastic feature in the case of a single SO line. The fact that it is instead almost twice is a good sign

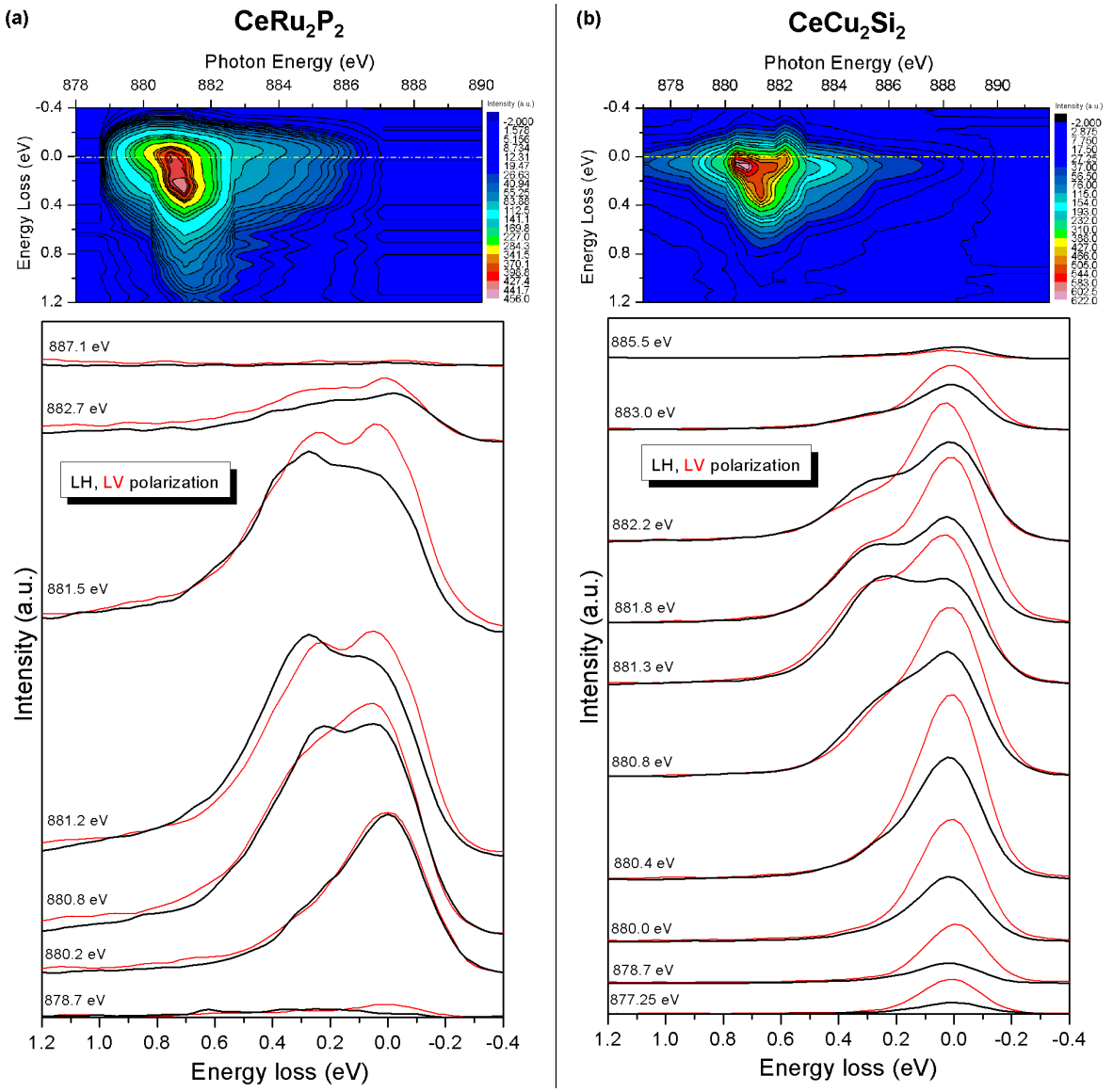

Figure 4.13: RIXS spectra of $CeRu_2P_2$ (*panel (a)*) and $CeCu_2Si_2$ (*panel (b)*) for different incident photon energies, increasing from bottom to top, around M_5 Ce edge, with LH (black) and LV (red) incident polarization. Spectra are aligned to their falling inflection point. Each spectrum comes from 30 min of acquisition. 2D color map are also shown for LH polarization. (measurement performed at ID08, ESRF).

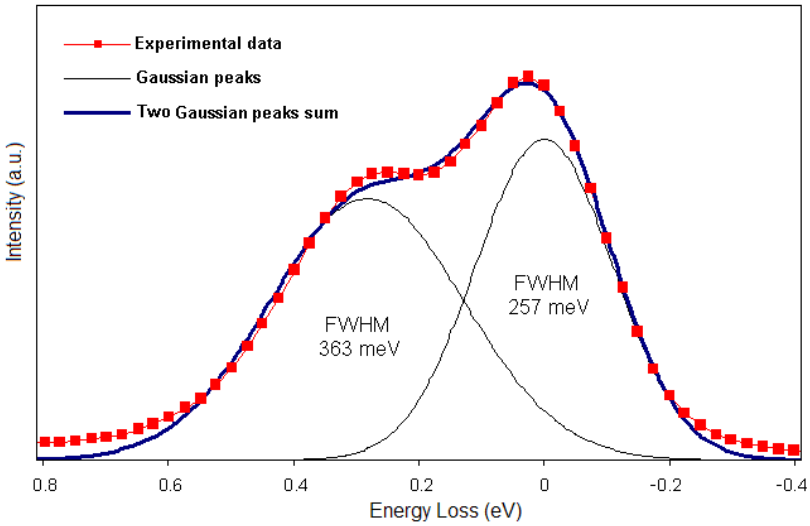

Figure 4.14: RIXS on $CeCu_2Si_2$ with LH polarization at 881.8 eV compared with a two Gaussian peaks spectrum (position 0 meV and 282 meV, FWHM of 257 meV and 363 meV respectively). Hints of CF substructures are observed because of the broadening of the inelastic feature larger than the spectrometer resolution (250 meV).

that those features are somehow substructured, even if we cannot resolve the level splitting.

Finally, it is remarkable that in addition to higher resolution measurements it would be useful a complete characterization of angular dependence, in order to identify possible dispersions. Both these requests will become available with the forthcoming beamline upgrade, as it will be shortly discussed in *Chapter 5*.

Scattering on the M_4 edge

We performed XAS and RIXS also on the M_4 Ce edge of the three sample. All the results are shown with 2D color maps in *Figure 4.16*, compared to the already shown M_5 edge scattering measurements. In NCCO only the elastic line is present, as expected: a $3d_{3/2}$ electron is excited into the $4f$ shell, and then it decades towards the core hole emitting a photon with energy equal to the incoming one, as well as on the M_5 edge.

On the other hand, in the case of Ce^{3+} samples the inelastic feature ascribable to jj excitation is much more suppressed if compared to the M_5 edge. This excitation is due to a transition from a state $|g\rangle$ with total momentum $J = 3/2$ to a state $|i\rangle$ with $J = 7/2$, and subsequent deexcitation. An absorption with $\Delta J = \pm 2$ involves a quadrupole transition, that is much more suppressed respect to the dipole transition, where $\Delta J = 0, \pm 1$ and corresponding in this case to an excitation in the $^2F_{5/2}$ state. However this is only a one-electron picture, which do not actually consider the multiplet structure of the states involved.

Finally it is noteworthy that the broadening of the quasi-elastic single feature of the spectra is larger than the spectrometer resolution also in this case, suggesting the presence of CF structure.

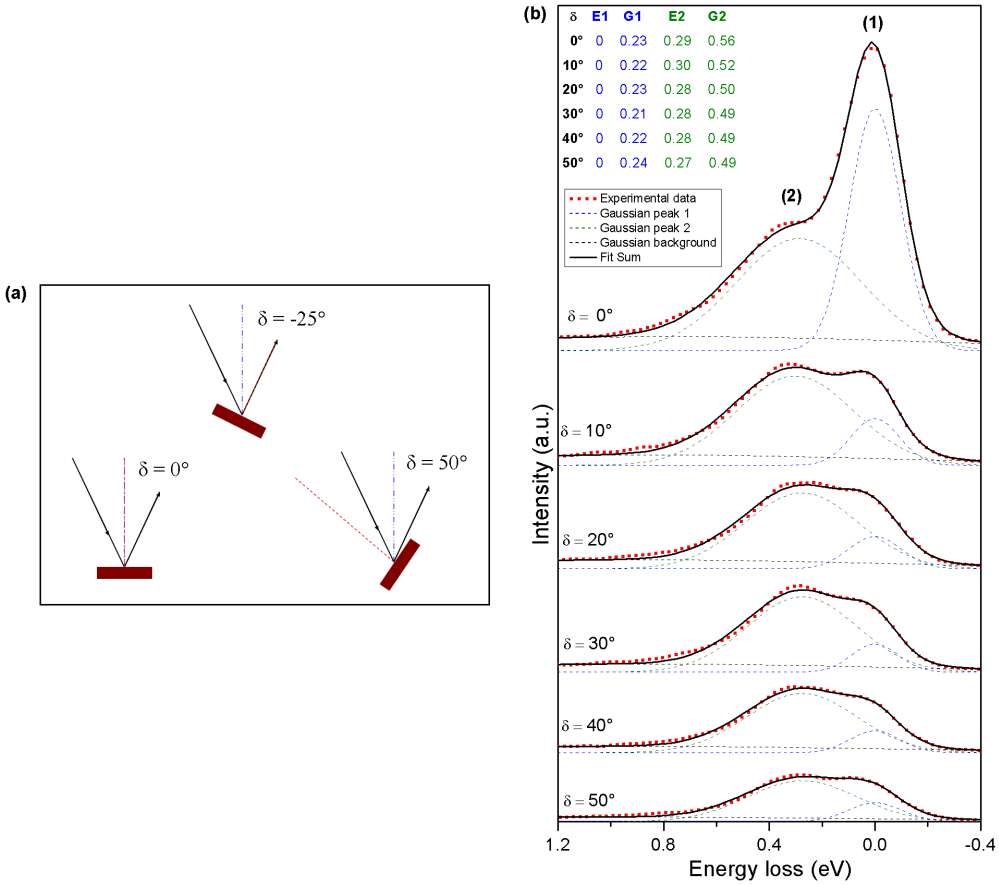

Figure 4.15: Angular dependence in RIXS. Panel (a): RIXS experimental setup. Energies were varied with normal emission ($\delta = -25°$). With fixed energy, incidence angle is varied from $\delta = 0°$ (specular angle) to $\delta = 50°$. Panel (b): RIXS spectra of $CeRu_2P_2$ at fixed 881.5 eV incident LH photon energy. Incident angle δ varies from 0° to 50°. All spectra (80 min of acquisition each) are aligned to their falling inflection point. Panel (c): two Gaussian spectra, one of them fixed at zero of energy loss, well fit the data. The second peak is almost constant in energy, but its FWHM is larger than the first one's.

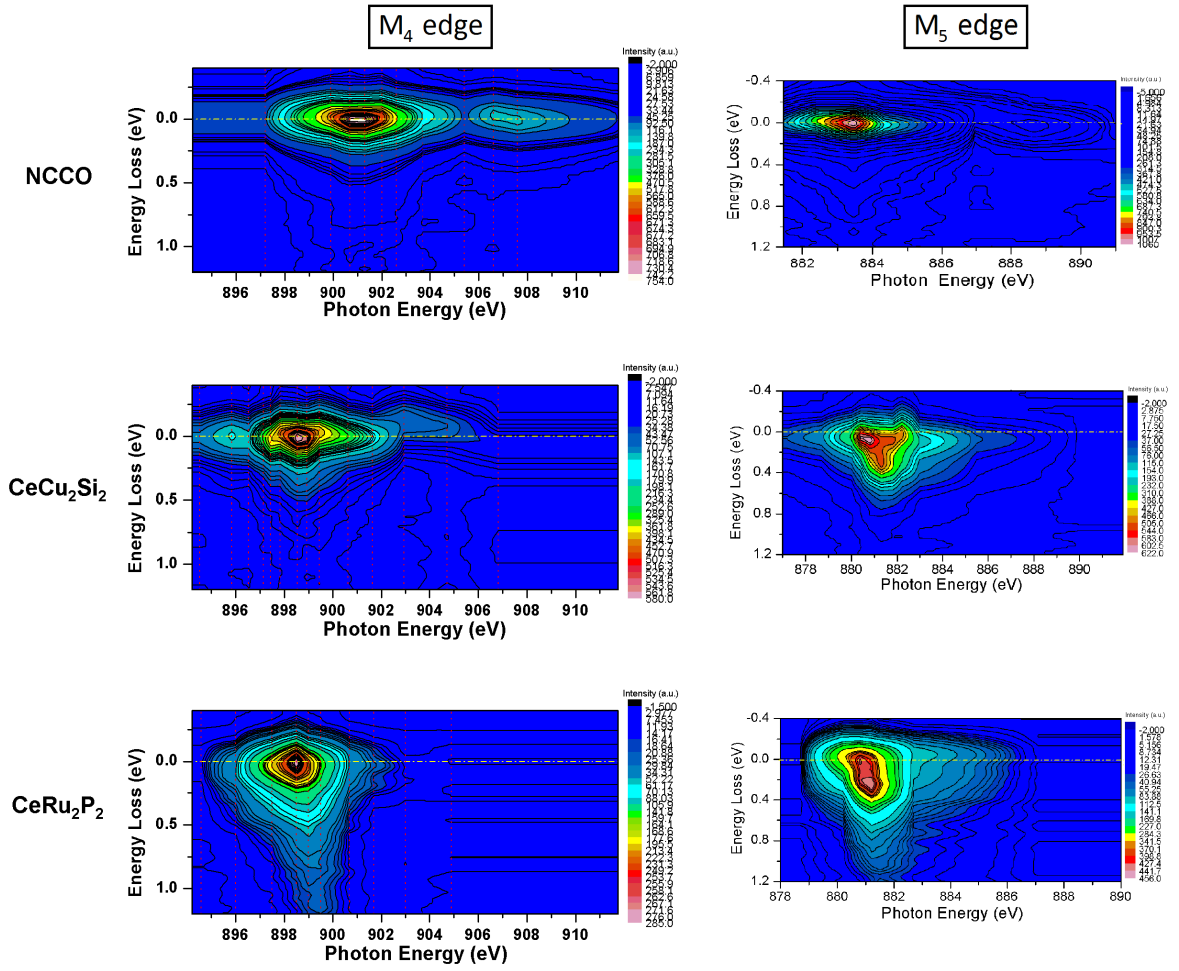

Figure 4.16: 2D color map of RIXS on M4 Ce edge in NCCO, $CeCu_2Si_2$ and $CeRu_2P_2$. Red dashed lines indicate the incident photon energies used in the measurements. A comparison with scattering on M_5 edge (from *Figure 4.12* and *4.13*) is shown on the right. Measurement performed at ID08, ESRF.

4.4 Energy Losses beyond the one eV range

Beyond the energy loss range of ~ 1 eV considered up to here, other two inelastic features are also observed, as it will be now reported.

4.4.1 Fluorescence emission features

As discussed in *Section 4.1*, Ce ions in NCCO sample are not actually isolated, and their ground state $|g\rangle$ in such compound is a superposition of $4f^0$ and $4f^1\underline{v}$ configurations. In this case the $4f$ electron comes from the hybridized Cu $3d$ valence band [29]. This is reflected in the absorption spectrum, where the resonance at the M_5 edge is splitted into two channels (see *Figure 4.1*). Therefore inelastic scattering becomes possible: in particular, depending on the excitation energy we can distinguish two cases.

If the $3d$ electron is promoted to a bounded $4f$ level, there is a finite probability that the core hole will be annihilated by the $4f$ electron coming from the ligand hybridization. This leaves the system with an exciton made by an $4f$ electron in the cerium site and a $3d$ hole in the copper site (green arrows in *Figure 4.17(a)*). Such excitation is known as *fd* Charge Transfer excitation (CT). The net energy transferred is fixed, independent from the incoming photon energy: in RIXS this is referred as *Stokes feature*, in analogy with the Raman process [1]. There is no clear sign of CT.

On the other hand, if the $3d$ electron is sent over the vacuum level into the continuum the $4f$ electron coming from the hybridization will decay on the $3d$ core hole (brown arrow in *Figure 4.17(a)*), but in this case no excitations are left in the system and is the outgoing photon energy being independent from the incident one, so that the energy loss will change linearly. In RIXS this is referred as *fluorescence emission feature* [1]. It is noteworthy that, in general, in addition to the hybridized $4f$ electron also delocalized electrons from $5d$ and $6s$ Ce valence band can make the fluorescence transition. In *Figure 4.17(b)* a RIXS 2D color map of NCCO is shown. A cyan line having $+1$ as angular coefficient well fits the trend of features arising around $4 \div 7$ eV of energy loss (see also *Figure 2.10*), so that they are identified as fluorescence features. Note that the three peaks of intensity exactly correspond to the incoming photon energy where data have been measured, simply suggesting a sort of artifact in the preparation of the map.

4.4.2 Coster-Kronig conversion

M_4 edge is at ~ 20 eV more than M_5, in fact a $3d_{3/2}$ electron is more bound than a $3d_{5/2}$, and thus it requires more energy to extract it. In this case after absorption the photon created core-hole has an additional channel of decaying: it can jump to the $3d_{5/2}$ level, i.e. an electron can decay from there; the gain in energy is given to an outer electron that is emitted from the material. In this case where two of the three Auger levels belong to the same orbital the transition is well known as *Coster-Kronig conversion* (CK) [39]. In particular, being involved two $3d$ levels and a $4f$ one, it is a CK conversion *MMN*-type (see *Figure 4.18(a)*).

Because of the additional decay channel the final state of absorption has a smaller lifetime, that entails a broader peaks in XAS spectra. Estimating a broadening of ~ 1 eV (see *Figure 4.1*), the lifetime is ~ 0.5 femtoseconds. CK conversion can be spotted also in RIXS in the form of high energy loss features: in fact a $4f$ electron can decay in the converted $3d_{5/2}$ core hole with a M_5 transition. In this case the difference between outgoing and incoming photon

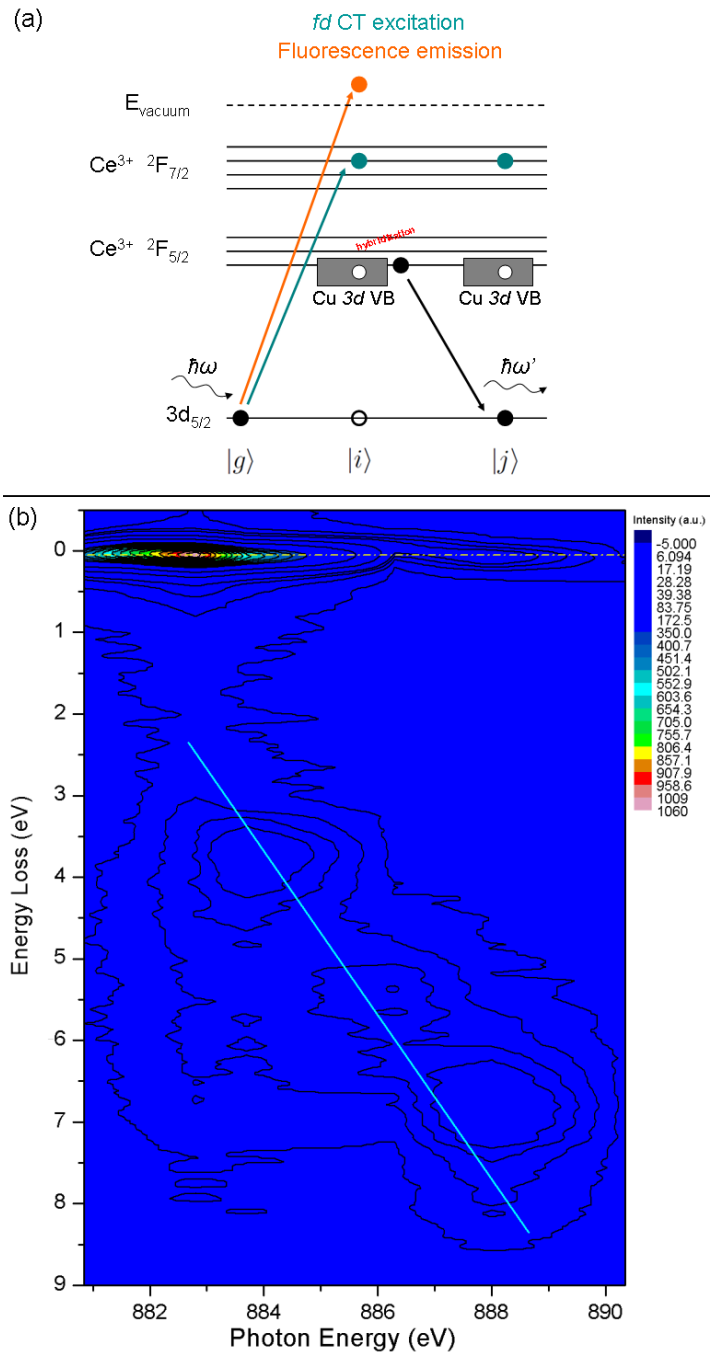

Figure 4.17: Panel (a): Scheme of Charge Transfer excitation and Fluorescence feature. Panel (b): 2D color map of RIXS measurements on NCCO at M_5 Ce edge, where red dashed lines indicate the photon energy used in the RIXS measurement, while other data are obtained by linear interpolation. Yellow dash-dotted line is the zero of the energy losses. Cyan line has -1 as angular coefficient. Fluorescence features are clearly visible. Measurement performed at ID08, ESRF.

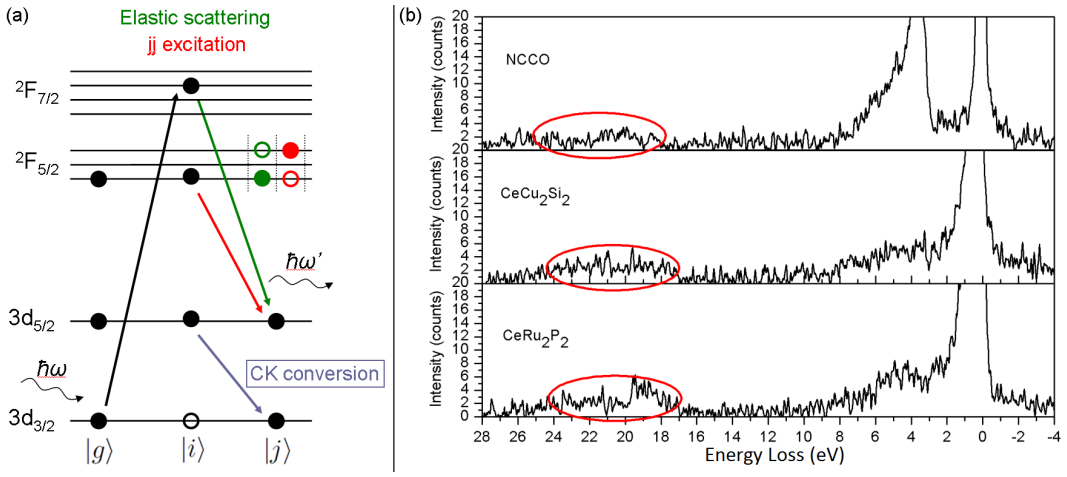

Figure 4.18: Coster-Kronig conversion in M_4 scattering. Panel (a): scheme of the process. Panel (b): RIXS measurements show a well-defined high energy loss in the three samples (measurement performed at ID08, ESRF).

energy is the difference between the two $3d$ levels, i.e. ~ 20 eV in our case. In *Figure 4.18(b)* is shown a RIXS spectrum of NCCO with 901.1 eV of resonant incoming photon energy and of $CeCu_2Si_2$ and $CeRu_2P_2$ with 899.1 eV. Around 20 eV a very weak but well defined feature arising from the background is visible, and can be attributed to CK conversion.

Chapter 5

Summary and Outlook

The present thesis is a study of Cerium compounds by means of resonant soft X-ray scattering. The electronic structure of Cerium is dominated by Spin-Orbit coupling, which produce a split between the ${}^2F_{5/2}$ ground state and the ${}^2F_{7/2}$ first excited state. Furthermore, the interaction with the Crystal Field generated by the surrounding charges produces a splitting of the $(2j+1)$-fold degeneracy because of a lowering of symmetry.

In the three samples we measured, $Nd_{1.84}Ce_{0.16}CuO_4$, $CeRu_2P_2$ and $CeCu_2Si_2$, the symmetry was the same, body-centered tetragonal. They differ in valence state, as we demonstrated with absorption measurements from M_5 and M_4 edge. In fact, a different valence of Cerium (4+, 3+ and a mixture of the two respectively) has been observed thanks to a comparison with reference samples. Differences between Fluorescence Yield and Auger Electron Yield have been interpreted in the light of the total emission spectrum. The presence of Crystal Field is suggested by a small Linear Dichroism and is supported by calculations.

By means of RIXS measurements on the M_5 edge we analyzed the excitations left in the samples involving two f levels (ff excitations). $Nd_{1.84}Ce_{0.16}CuO_4$, having a Ce^{4+} ion, has $|4f^0\rangle$ configuration, thus inelastic scattering involving different f electrons is not possible. Coherently, we measured only the elastic line in the low energy range of RIXS spectra. In addition, a clear fluorescence feature due to the hybridized $|4f^1\underline{v}\rangle$ configuration was observed, identified from its linearly dependence on the incoming photon energy. In the other two samples $CeCu_2Si_2$ and $CeRu_2P_2$, having $|4f^0\rangle + |4f^1\rangle$ and $|4f^1\rangle$ configuration respectively, we measured an inelastic associated to a Spin-Orbit excitation, i.e. an excitation between two f levels with different total momentum J (jj excitation). Neither excitations among Crystal Field splitted levels with same J nor their dispersion with momentum have been clearly observed because of lack of resolution. Nevertheless, the broadening of RIXS features was much larger than the spectrometer resolution, thus suggesting an effective Crystal Field substructure. It is noteworthy that our measurements are in a good agreement with atomic multiplet calculations. We measured also the scattering from the M_4 edge and the spectra show the same qualitative results, even if jj excitations are very suppressed, with in addition a high energy loss due to MMN Coster-Kronig conversion.

The measure of the $4f$ SO splitting in Cerium we obtained is 300 meV, which is in agreement with ARPES measurements [7]. RIXS however, being a photon-in/photon-out and thus charge neutral technique, can be considered as a more direct way to probe the electronic structure.

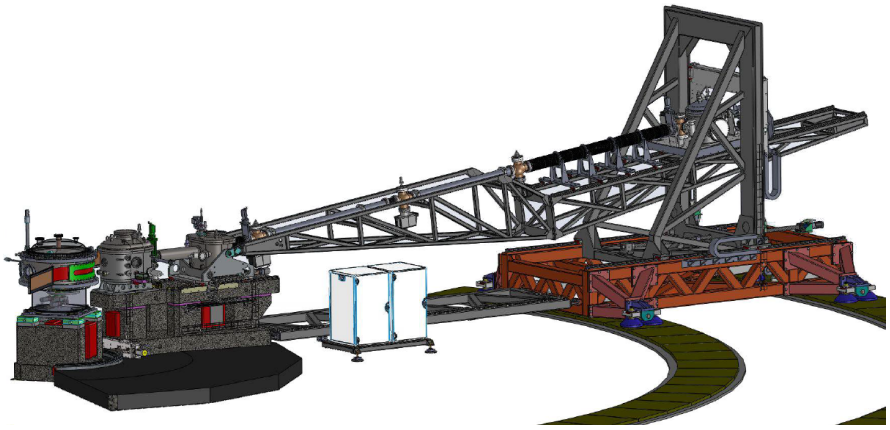

Figure 5.1: Scheme of ϵRIXS, the high resolution spectrometer that will be installed in 2014 at ID32, ESRF.

The RIXS spectra we measured are well consistent with calculations performed with CF parameters obtained by Inelastic Neutron Scattering [8]. Therefore, even if we cannot actually resolve the CF structure, this is a proof that it can be measured by RIXS in general, if the resolution is sufficient. The advantage of RIXS compared to Neutron Scattering is that the photon beam size is of the order of a few tens of micrometers, so that only small quantities of sample are needed. This is important when single crystals are difficult to be prepared, and extreme thermodynamic conditions become also achievable. In addition, with neutrons it is difficult to measure losses higher than ~ 100 meV. In the case of $CeCu_2Si_2$, for example, SO features are not detectable, as shown in *Figure 1.4*.

In this perspective the construction of a new groundbreaking spectrometer is remarkable: in 2014 the ID08 beamline will be moved to ID32 where the new European Resonant Inelastic X-ray Spectrometer (ϵRIXS) is expected to be commissioned by the end of the year (see *Figure 5.1*). The upgrade consists mainly of two features.

The first is the energy resolution. Thanks to a 110 m long beamline and to an entrance and exit arms of the spectrometer long 2.4 m and 8.6 m respectively the estimated resolution will be higher than $E/\delta E = 30000$ at 930 eV. This means that 250 meV of current resolution on Ce M_5 edge will improve to 30 meV. This value is smaller than the typical Crystal Field splitting energy, therefore CF excitations are supposed to be clearly visible. Thus our results open the way to new promising studies on low energy excitations in $4f$ materials. For instance, it would be also interesting to study other Rare Earths with more than one electron in the $4f$ shell: in this case other excitations, like spin excitations, become possible.

The second important upgrade is the continuous rotation over 100° of the spectrometer itself. In the current setup the spectrometer is fixed at 50° from the incoming beam, and only the sample holder can rotate, i.e. is possible to vary the incidence angle but not the scattering one. In other setups is possible to obtain only few discrete variations of the scattering angle. On the other hand, with ϵRIXS it will be possible to change simultaneously both the incidence and the scattering angles. This means that, once the CF will be identified, it will become possible for the first time to finely study their dispersion over the whole Brillouin Zone.

The dispersion of CF excitations should strongly influence the transport properties of $4f$ materials, and a direct measure of it would represent an important breakthrough in the understandings of Rare Earth compounds and strongly correlated materials in general.

Bibliography

[1] L. J. P. Ament, M. van Veenendaal, T. P. Devereaux, J. P. Hill and J. van den Brink, "Resonant Inelastic X-ray Scattering studies of elementary excitations"
Rev. of Modern Physics, vol.83 (2011)

[2] J. Quintanilla and C. Hooley, "The strong-correlations puzzle"
Phys. World 22, 32-37 (2009)

[3] J. Bardeen, L. N. Cooper and J. R. Schrieffer, "Theory of Superconductivity"
Phys. Rev. E 108,5 (1957)

[4] L. Braicovich, G. Ghiringhelli and A. Tagliaferri, "Inelastic resonant M-scattering of X-rays from Gd metal with inner-shell excitation"
Il Nuovo Cimento 20, 7-8 (1998)

[5] J. Jensen and A. R. Mackintosh, "Rare Earth Magnetism - Structures and Excitations"
Oxford University Press, ISBN 0198520271

[6] D. V. Vyalikh, S. Danzenbächer, Yu. Kucherenko, K. Kummer, C. Krellner, C. Geibel, M. G. Holder, T. K. Kim, C. Laubschat, M. Shi, L. Patthey, R. Follath and S. L. Molodtsov, "k dependence of the Crystal Field splittings of $4f$ states in Rare Earth systems"
Phys. Rev. Lett. 105, 237601 (2010)

[7] D. V. Vyalikh et al.,
Unpublished

[8] E. A. Goremychkin and R. Osborn, "Crystal-field excitations in $CeCu_2Si_2$"
Phys. Rev. B 47, 21 (1993)

[9] F. de Groot and J. Vogel, "Fundamentals of X-ray absorption and dichroism: the multiplet approach"
Springer, ISBN 978-1-4020-3337-7

[10] F. de Groot and A. Kotani, "Core Level Spectroscopy of Solids"
Advances in Condensed Matter Science vol.6, CRC Press, Taylor & Francis Group, ISBN 978-0-8493-9071-5

[11] R. M. Eisberg and R. Resnick, "Quantum physics of atoms, molecules, solids, nuclei, and particles"
John Wiley & Sons Inc., ISBN 0-471-87373-X

[12] Center for X-Ray Optics, LBNL, "X-ray Database"
www.cxro.lbl.gov/

[13] M. Newville, "Fundamentals of XAFS"
http://xafs.org/Tutorials

[14] J. E. Penner-Hahan, "X-ray Absorption Spectroscopy"
http://www.umich.edu/~jphgroup/XAS_Course/

[15] F. de Groot, "Multiplet effects in X-ray Spectroscopy"
Coord. Chem. Rev. 249, 3163 (2005)

[16] J. Stöhr, "NEXAFS spectroscopy"
Springer, ISBN 3-540-54422-4

[17] A. Kotani and S. Shin, "Resonant Inelastic X-ray Scattering spectra for electrons in solids"
Reviews of Modern Physics, vol.73 (2001)

[18] H. Yavaş, M. van Veenendaal, J. van den Brink, L. J. P. Ament, A. Alatas, B. M. Leu, M.-O. Apostu, N. Wizent, G. Behr, W. Sturhahn, H. Sinn and E. E. Alp, "Observation of phonons with resonant inelastic x-ray scattering"
J. Phys. Condens. Matter 22, 485601 (2010)

[19] L. Braicovich, J. van den Brink, V. Bisogni, M. Moretti Sala, L. J. P. Ament, N. B. Brookes, G. M. De Luca, M. Salluzzo, T. Schmitt, V. N. Strocov and G. Ghiringhelli, "Magnetic Excitations and Phase Separation in the Underdoped La(2-x)Sr(x)CuO(4) Superconductor Measured by Resonant Inelastic X-Ray Scattering"
Phys. Rev. Lett. 104, 077002 (2010)

[20] C.-C. Kao, W. A. L. Caliebe, J. B. Hastings and J.-M. Gillet, " X-ray resonant Raman scattering in NiO: Resonant enhancement of the charge-transfer excitations"
Phys. Rev. B 54, 1636116364 (1996)

[21] M.Nakazawa, H. Ogasawara and A. Kotani, "Theory of polarization dependence in resonant X-ray emission spectroscopy of Ce compounds"
J. Phys Soc. Japan, vol.69, no.12, 4071-4077 (2000)

[22] J. D. Jackson, "Classical Electrodynamics"
John Wiley & Sons Inc., ISBN 0-471-43131-1

[23] E. E. Koch, "Handbook on Synchrotron Radiation"
Vol 1a, North Holland, ISBN 0444867090

[24] M. Minola, "Magnetic, orbital and charge fluctuations in layered cuprates studied by RIXS"
PhD Thesis (2013), http://hdl.handle.net/10589/74562

[25] C. T. Chen and F. Sette, "Performance of the Dragon soft X-ray beamline"
Rev. Sci. Instrum. 60, 1616 (1989)

[26] C. Dallera, E. Puppin, G. Trezzi, N. Incorvaia, A. Fasana, L. Braicovich, N. B. Brookes and J. B. Goedkoop, "Soft X-ray Emission Spectroscopy at ESRF Beamline 26 based on a helical undulator"
J. Synchrotron Rad. 3, 231-238 (1996)

[27] M. E. Dinardo, A. Piazzalunga, L. Braicovich, V. Bisogni, C. Dallera, K. Giarda, M. Marcon, A. Tagliaferri and G. Ghiringhelli, "Gaining efficiency and resolution in soft x-ray emission spectrometers thanks to directly illuminated CCD detectors"
Nucl. Instrum. Methods Phys. Res., Sect. A, vol. 570, p. 176 (2007)

[28] C. Q. Jin, Y. S. Yao, B. Q. Wu, Y. F. Xu, S. C. Liu and W. K. Wanga, "Superconductivities of ntype $Nd_{1.85}Ce_{0.15}CuO_{4-y}$ prepared under high pressure"
Appl. Phys. Lett. 59, 3479 (1991)

[29] G. C. Rout, B. N. Panda and S. N. Behera, "Mutual influence of superconductivity and magnetism in strongly correlated cuprates"
Physica C 333, 104120 (2000)

[30] F. Steglich, H. Aarts, C. Bredl, W. Lieke, D. Meschede, W. Franz and H. Schfer, "Superconductivity in the presence of strong Pauli paramagnetism: $CeCu_2Si_2$"
Phys. Rev. Lett. 43, 18921896 (1979)

[31] R. Lässer, J. C. Fuggle, M. Beyss, M. Campagna, F. Steglich and F. Hulliger, "X-ray Photoemission from Ce core levels of $CePd_3$, CeSe, $CeAl_2$ and $CeCu_2Si_2$"
Physica 102B, 360-366 (1980)

[32] P. Fulde and M. Loewenhaupt, "Magnetic excitations in crystal-field split $4f$ systems"
Adv. in Phys. 34:5, 589-661 (1985)

[33] Center for X-Ray Optics, LBNL, "X-ray Data Booklet"
www.cxro.lbl.gov/

[34] S. Eisebitt, T. Böske, J.-E. Rubensson and W. Eberhardt, "Determination of absorption coefficients for concentrated samples by fluorescence detection"
Phys. Rev. B 47, 14103 (1992)

[35] M. Pompa, A. M. Flank, P. Lagarde, J. C. Rife, I. Stekhin, M. Nakazawa, H. Ogasawara and A. Kotani, "Experimental and theoretical comparison between absorption, total electron yield and fluorescence spectra of rare-earth M5 edges"
Phys. Rev. B 56, 2267 (1997)

[36] L. Braicovich, A. Tagliaferri, E. Annese, G. Ghiringhelli, C. Dallera, F. Fracassi, A. Palenzona and N. B. Brookes, "Spectroscopy of strongly correlated systems: resonant xray stcattering without energy resolution in scattered beam"
Phys. Rev. B 75, 073104 (2007)

[37] Y. Ma, "X-ray absorption, emission, and resonant inelastic scattering in solids"
Phys Rev. B 49, 5799 (1994)

[38] R. Gusmeroli and C. Dallera, "Missing 1.1"
http://www.esrf.eu/computing/scientific/MISSING/

[39] D. Coster and R. de L. Kronig, "New type of auger effect and its influence on the x-ray spectrum"
Physica 2, 1-12, 1324 (1935)

Acknowledgements

At the end of my studies I would like to thank, first of all, Prof. Giacomo Ghiringhelli from Politecnico di Milano and Dr. Nicholas Brookes from ESRF, for their helpfulness, competence and kindness. They also gave me the great opportunity of doing my traineeship in ID08 beamline at ESRF. It has been really pleasing working there, and I am so glad to be the last trainee of the long story of AXES*, which is now retired (and long live* ϵRIXS*!).*

Then I would like to thank Dr. Kurt Kummer, for his precious support, his strong dedication and, most of all, his patience with me. I have been adviced with competence since the first day of traineeship, in a very nice, friendly and professional way.

Thanks also to the beamline staff: Flora and, in order of desk rigorously, Eimear, Julian, Andrea, Mathieu, Marcio, Erika, Patrick. You all made a good day even the hardest day. And thanks to Greta, too, especially for his company during beam times: days, nights, and even Easter.

Thanks to the group of S. Seiro, N. Caroca-Canales and C. Geibel from Max Planck Institut für Chemische Physik fester Stoffe, Dresden, for preparing the samples we measured, and thus permitting us to perform the experiments discussed in the present thesis.

A particular thanks to Prof. Lucio Braicovich, for his amazing enthusiasm, boundless knowledge and helpful advices. Thanks also to all the Professors I met during my studies, for giving me a scientific, technical and also personal education.

Thanks to all the people with whom I had a really good time during these five years, in Milano, in Paris, in Grenoble, and thanks to whom has always been close to me.

Finally, a special thanks to my Parents: they have always supported and encouraged me since I was born, with confidence, comprehension and love. Thanks for everything.